

**ELECTROMAGNETIC DECAY OF THE
SECOND EXCITED STATE OF C^{12}**

**Thesis by
Philip A. Seeger**

**In Partial Fulfillment of the Requirements
For the Degree of
Doctor of Philosophy**

**California Institute of Technology
Pasadena, California**

1963

ACKNOWLEDGEMENTS

I wish to thank Dr. R. W. Kavanagh for his great help in the conception, design, and execution of this experiment. I am also indebted to the entire staff of the Kellogg Radiation Laboratory, not only for many useful discussions and suggestions, but also for creating an atmosphere in which the work could be successfully carried out.

ABSTRACT

It was desired to determine what fraction of C^{12} nuclei in the second excited state decay electromagnetically to the ground state instead of by alpha emission. The state was formed with the reaction $N^{14}(d,\alpha)C^{12*}$ by bombarding a thin vanadium nitride target on carbon foil with 1.8-MeV deuterons. Recoil C^{12} nuclei were observed in coincidence with the alpha particles from the reaction. The alphas were detected with a surface-barrier counter set at the appropriate unique angle, and the recoiling nuclei at 90° were analyzed in momentum with a magnetic spectrometer, in energy by a surface-barrier counter at the spectrometer focus, and in velocity by the time delay between the alpha and the C^{12} counts. Pulses of 40-nsec width were recorded photographically from a Tektronix type 555 dual-beam oscilloscope, providing a time resolution of 5 nsec, and also allowing pulse height analysis on the fast pulses. Of the C^{12} nuclei formed in the second excited state, 99.9+ per cent decay by alpha emission to Be^8 and are not detected; only those which decay to the C^{12} ground state by gamma or pair emission will be seen. Thus the experiment provides a direct measurement of Γ_{rad}/Γ . The value of $\Gamma_{rad} = (\Gamma_\gamma + \Gamma_{e\pm})$ has astrophysical significance, determining the rate of C^{12} formation in the He-burning process in red giant stars. Analysis of 170 observed events gives $\Gamma_{rad}/\Gamma = (2.8 \pm 0.3) \times 10^{-4}$. Averaged with a value of $(3.3 \pm 0.9) \times 10^{-4}$ obtained by Alburger, and combined with a value of $\Gamma = (8 \pm 5) \text{ eV}$, the result is $\Gamma_{rad} = (0.0024 \pm 0.0015) \text{ eV}$, which is two-and-one-half times the value used in previous astrophysical calculations.

TABLE OF CONTENTS

PART	TITLE	PAGE
I.	INTRODUCTION	
	A. Astrophysical Significance	1
	B. Previous Knowledge	3
II.	EXPERIMENT; APPARATUS	
	A. Reasons for Using $N^{14}(d,\alpha)C^{12*}$; Kinematics	5
	B. Target Manufacture	6
	C. Recoil-Ion Detection	7
	D. Alpha Detection	9
	E. Coincidence Detection	12
III.	PROCEDURE AND RESULTS	
	A. Non-Coincident Recoil-Ion Spectra	16
	B. Non-Coincident Alpha Spectra	16
	C. Procedure for Recording Coincidences	17
	D. Energy and Time Normalization	19
	E. Determination of Number of Counts	22
	F. Experimental Results	24
IV.	ANALYSIS OF RESULTS	
	A. Equation for Γ_{rad}/Γ	26
	B. Population Factor, P	28
	C. Charge State Factor, C	28
	D. Geometry Factor, G	31
	E. Thickness Factor, T	34
	F. Calculation of Γ_{rad}/Γ	36
V.	CONCLUSION	37

TABLE OF CONTENTS (Cont'd)

	PAGE
APPENDICES	
A. Thin Nitrogen Targets	
1. Carbon-foil backing	40
2. Vanadium evaporation	40
3. Nitriding	41
4. Composition.	42
B. Camera and Film Developing	44
C. Momentum of Gamma Rays	
1. First excited state	46
2. Second excited state	47
D. Projection of a Rectangle in Spherical Co-ordinates . .	50
REFERENCES	55
TABLES	59
FIGURES	71

I. INTRODUCTION

A. Astrophysical Significance

A star which has converted most of its hydrogen into helium will undergo gravitational contraction either until an instability arises or until the central temperature is raised to such a level that a new nuclear fuel is available as a source of energy. Salpeter (1952, 1957) has pointed out that at temperatures of the order of 10^8 °K, the reactions



will produce small amounts of Be^8 and C^{12*} in dynamic equilibrium. The level of C^{12} involved has an interesting history, summarized by Cook (1957). When experiments established that the ground state of Be^8 is unbound by only 95 ± 5 keV (Hemmendinger 1948, Tollestrup 1949), Salpeter (1952) calculated an equilibrium ratio of Be^8 to He^4 of the order of 10^{-9} for red giant stars. The effect of the resonance in $\text{He}^4 + \text{He}^4$ was to increase the helium-burning reaction rate compared to non-resonant calculations by Öpik (1951, 1953), but the Salpeter calculations still did not give a fast enough reaction rate at 3×10^8 degrees. Hoyle (1954) predicted the existence of a level in C^{12} at 7.70 MeV, on the basis of considerations of reaction rates and of the relative abundances of He^4 , C^{12} , and O^{16} . At the time of Hoyle's prediction there was conflicting evidence regarding the existence of such a state. A subsequent experiment (Hoyle 1953, Dunbar 1953) using the reaction

$N^{14}(d, \alpha)C^{12*}$ with a high-resolution magnetic spectrometer to observe the alpha groups, clearly identified an alpha-particle group leading to the state in question. In Figure 1 (Lauritsen 1962) the state is shown at 7.656 MeV, very close to the position predicted by Hoyle. Cook (1957) showed that this state does indeed decay into three alpha particles through an intermediate stage involving He^4 and the ground state of Be^8 , proving (by the general reversibility of nuclear reactions) that the reactions of equation 1 can occur.

If a C^{12*} decays electromagnetically to the ground state, either by gamma emission, by pair emission, or by gamma cascade through the first state, the net result will be (Everling 1960)



The purpose of this experiment was to find the total electromagnetic decay width of the 7.656-MeV state of C^{12} .

If the probability of leakage to the ground state is small compared to the alpha emission by C^{12*} indicated in equation 1, the equilibrium can be expressed (Salpeter 1957) by the law of mass action as for a triatomic molecule:

$$n_* = n_\alpha^3 \frac{(2J_* + 1)}{(2J_\alpha + 1)^3} \left(\frac{2\pi\hbar^2}{M_\alpha kT} \right)^{3/2} \exp\left(-\frac{E_r}{kT}\right), \quad (3)$$

where n_* = number density of C^{12*} ,

J_* = spin of $C^{12*} = 0$,

n_α = number density of He^4 ,

J_α = spin of $He^4 = 0$,

M_α = mass of He^4 ,

E_r = energy difference $(C^{12*} - 3 He^4)c^2 = 372 \text{ keV}$ (Cook 1957).

The rate of reaction 2 is then given by

$$P = n_* \frac{\Gamma_{\text{rad}}}{\hbar} \quad , \quad (4)$$

since the mean lifetime for electromagnetic decay is $\hbar/\Gamma_{\text{rad}}$, where Γ_{rad} is the total radiative decay width. The energy generation per unit time and per unit mass is

$$\epsilon = \frac{PQ}{\rho} = 1.386 \times 10^{24} \rho_5^2 x_\alpha^3 f \frac{\Gamma_{\text{rad}}}{T_8^3} \exp\left(-\frac{43.2}{T_8}\right) \frac{\text{erg}}{\text{g sec}} \quad , \quad (5)$$

where $\rho_5 = \rho \times 10^{-5} = \text{density in } 10^5 \text{ g/cm}^3$,

Γ_{rad} is in eV,

$x_\alpha = \text{mass fraction of He}^4$,

$T_8 = \text{temperature in } 10^8 \text{ }^\circ\text{K}$,

$f \approx \exp\left[0.88 \left(\frac{\rho_5}{T_8}\right)^{\frac{1}{2}}\right]$.

The factor f is an electron screening correction (Salpeter 1954, B²FH 1957) necessary when $\frac{\rho_5}{T_8} \gtrsim 0.1$. From equation 5 we see that energy production by the Salpeter process is linearly dependent on Γ_{rad} .

B. Previous Experimental Evidence

From the work of Cook et al. (1957) as well as later experiments (Alburger 1960, Ajzenberg-Selove 1960), the spin and parity of the 7.656-MeV level are almost certainly 0^+ . Hence direct gamma decay to the 0^+ ground state is strictly forbidden, and has not been observed. Both pair emission to the ground state and the gamma cascade through the 2^+ first excited state have been observed.

Although earlier experiments (Kavanagh 1958, Eccles 1959) had

only been able to place an upper limit of 0.1% on the ratio $\Gamma_{\gamma}/\Gamma_{\alpha}$, a recent experiment by Alburger (1961) gave a positive result. Observing p- γ - γ triple coincidences in the reaction $B^{10}(\text{He}^3, p)C^{12*}(\gamma\gamma)C^{12}$ (see Figure 1) he obtained for the branching ratio of the 3.223-MeV γ -ray to the first state:

$$\Gamma_{3.2\gamma}/\Gamma_{\alpha} = (3.3 \pm 0.9) \times 10^{-4} . \quad (6)$$

A previous set of experiments (Alburger 1960, Ajzenberg-Selove 1960) gave the branching ratio for pair emission:

$$\Gamma_{e\pm}/\Gamma_{\alpha} = (6.6 \pm 2.2) \times 10^{-6} . \quad (7)$$

In addition, an absolute value of $\Gamma_{e\pm}$ can be calculated (Oppenheimer 1939) from a knowledge of the EO matrix element obtained (Schiff 1955) from inelastic electron scattering data (Fregeau 1956):

$$\text{M. E.} = (5 \times 10^{-26}) \pm 25\% ,$$

$$\Gamma_{e\pm} = (5\frac{1}{2} \pm 3) \times 10^{-5} \text{ eV} . \quad (8)$$

Combining these results gives

$$\Gamma = (8 \pm 5) \text{ eV} , \quad (9)$$

$$\Gamma_{\text{rad}} = (0.0027 \pm 0.0018) \text{ eV} . \quad (10)$$

The present experiment provides a completely independent measurement of the ratio $\Gamma_{\text{rad}}/\Gamma$, but requires an estimate of Γ in order to give Γ_{rad} itself. At present, equation 9 is the best experimental value of Γ .

II. EXPERIMENT; APPARATUS

A. Reasons for Using $N^{14}(d, \alpha)C^{12*}$; Kinematics

The plan of the experiment was to populate the second state of C^{12} in a nuclear reaction, and to observe carbon ions recoiling from the reaction. Since the lifetime of the state is known from the alpha width to be of the order of 10^{-16} seconds, and it takes 1.8×10^{-9} seconds for a 2-MeV C^{12} to travel 1 cm, the recoils can be detected only if radiative decay has occurred. To distinguish C^{12} ions from other reaction products, a low-resolution magnetic spectrometer was to be used. Since it was necessary to impart as much momentum as possible to the recoil nucleus, using a 2-MeV Van de Graaff accelerator, a reaction with a high Q-value and with a heavy (e.g., mass 4) emitted particle was sought. From Figure 1 two reactions are seen to qualify:

$$C^{13}(He^3, \alpha)C^{12}, \quad Q_0 = 15.630 \text{ MeV};$$

$$N^{14}(d, \alpha)C^{12}, \quad Q_0 = 13.574 \text{ MeV}.$$

The second of these reactions was chosen because a natural nitrogen target could be used; the C^{13} reaction would require an enriched target. Also, the fact that the energy loss of deuterons in the target would be much less than He^3 nuclei would allow us to use higher beam intensities for a given target thickness and temperature. Further, the second state of C^{12} was known to be populated in the $N^{14}(d, \alpha)$ reaction (Hoyle 1953, Dunbar 1953), and presumably has a higher cross section.

A schematic diagram of the equipment used is shown in Figure 2. With a deuteron bombarding energy of 1.800 MeV, recoil carbon ions at 90° in the laboratory system have an energy of 3.6 MeV for ground-state reactions, and 2.5 MeV or 1.7 MeV if the first or second excited states are formed. The corresponding alpha-particle energies and angles, and also the flight time t of the C^{12} ions through the 85-cm path length of the spectrometer, are given in Table I. Recoil ions of the proper momentum and energy were observed in delayed coincidence with alpha particles of the proper energy and angle, the delay being equal to the proper flight time for the ion. The two pulses (C^{12} and α) were displayed on a dual-beam oscilloscope and photographed.

B. Target Manufacture

Target requirements for this experiment were stringent. Because of the low yield, it was desired to have a high N^{14} content; however the active layer had to be kept thin for the recoil ions. The calculated stopping power of VN (vanadium nitride) for 1.7-MeV C^{12} ions is about 400×10^{-15} eV cm^2 /molecule; hence the maximum allowed target thickness for VN would be about 10^{18} molecules/ cm^2 for a 10% energy loss in the target. The backing of the target had to be transparent to the emerging alpha particles, yet strong enough to withstand the beam and the target-making procedure.

Organic materials, such as adenine ($C_5N_5H_5$), although attractive because of their high nitrogen content, had to be discarded because of their inability to withstand high temperatures.

Among the refractory metallic nitrides, gallium nitride was thought to sublime without decomposing (Gmelin 1936, Sime 1956). However, all attempts at vacuum evaporation at temperatures from 950 °C to 1400 °C resulted in decomposition; no nitrogen could be detected on the targets. An attempt to evaporate silicon nitride failed similarly.

Usable VN targets were made by evaporating vanadium onto mounted C foils, and nitriding by heating in an atmosphere of ammonia. An alpha-particle beam was used to heat the target. (See Figure 3.) The process is described in detail in Appendix A. The same procedure was tried with silicon, but apparently the temperature was not sufficient to cause nitriding. When titanium was evaporated onto carbon foils, they invariably broke, but some success was realized with Ti by evaporating before the foils were mounted.

Target composition was checked by elastically scattering 1-MeV protons from the target at a laboratory angle of 150°. Using a 10½-inch double-focusing magnetic spectrometer, the protons scattered from different masses in the region of interest were well resolved. Figure 4 shows the profile of a typical target, and Table II lists the compositions of the various targets used during the experiment. Details of the calculation are included in Appendix A.

C. Recoil-Ion Detection

The alternating-gradient magnetic spectrometer indicated in Figure 2 has been described by Martin and Kraus (1956). The entrance slit of the magnet is elliptical with the major axis vertical. Being

5/32 inch wide, 0.963 inch tall, and 3.25 inches from the target, it subtends a solid angle of 0.011 steradians, yet has a mean width in the reaction plane of only 2.4° . The path length through the magnet from target to detector is 85 cm. An image slit 1/8 inch wide was used for most of the experiment. The elastic-scattering edge of protons from a gold foil showed a momentum resolution of 5% for this slit. This large value of $\Delta p/p$ was very useful to obtain a reasonable counting rate. For calibration, a 1/32-inch slit was also used; the gold scattering indicated a resolution of 1.3% for this narrower slit.

With the axis of the entrance aperture of the magnet set at a lab angle of 90° , the object position was determined by finding the maximum counting rate with respect to motion of the beam spot. A B^{10} target was bombarded with 1.17-MeV protons; 1.37-MeV alpha particles from the reaction $B^{10}(p, \alpha_0)Be^7$ were detected at the focus of the magnet, and 431-keV gamma rays from $B^{10}(p, \alpha_1\gamma)Be^7$ were used as monitor counts. Beam position (vertical and east-west) could be measured to within 0.003 inch on a quartz disk at the rear of the chamber; north-south motion was measured by turnscrews. Only vertical motion of the beam spot seriously affected the counting rate; a deviation of 1/32 inch either direction from the optimum position reduced the counting rate to one-half. A similar motion in either horizontal direction had only a 15% effect. A beam spot approximately 1/16 inch high and 1/32 inch wide (1/16 inch square on the target) was used during the experiment.

The detector at the magnet focus was a 7 x 14-mm gold-silicon surface-barrier detector manufactured by Oak Ridge Technical Enterprises Corporation (ORTEC). Initially counters made in this laboratory were used, but the commercial unit was installed before any data were obtained.

The pulse from the detector was amplified as shown in Figure 2 by a fast-amplifier system consisting of a single triode (417A) pre-amplifier and four Hewlett-Packard type 460A wide-band amplifiers. At the input to the second amplifier the pulse was clipped to 40-nsec width with a shorted length of 93-ohm cable. The amplified positive pulse was fed to the coincidence mixer and to the lower-beam input of a Tektronix type 555 dual-beam oscilloscope. The pulse height was about 1 volt for a 3-MeV particle; a vertical deflection of 0.5 V/cm was used. On the lower beam in Figure 5b, the two groups are deuterons (1.13 MeV) and alpha particles (2.27 MeV).

The pulse from the detector was also fed through a 1000-ohm resistor to a low-noise integrating preamp (ORTEC type 100A). The preamp output was connected to the internal amplifier of a 400-channel analyzer (Radiation Instruments Development Laboratories type 34-12). These are also shown in Figure 2.

D. Alpha Detection

The target chamber used for the experiment (see Figure 6) has provision for continuous variation of the angle θ from 35° to 90° . Since it was built before solid-state detectors were developed, it was designed for use with a CsI crystal and a photomultiplier extending

outside the chamber through a slot, with an O-ring as a sliding vacuum seal. In any currently designed chamber, the counter would more logically be mounted completely within the chamber, on a rotating arm concentric with the target rod.

A rectangular slit is mounted in the counter holder to define the solid angle of the alpha detector. A slit 0.032 inch wide and 0.200 inch high, about the same solid angle as the spectrometer aperture, was used in early runs, but eventual substitution of a slit 0.060 inch wide increased the coincidence counting rate and decreased the dependence on the determination of the angle θ . The effect of this change is discussed in section IV D below.

Gold-silicon surface-barrier detectors were made according to the recipe of Dearnaley and Whitehead (1961). However after commercial counters were obtained for use at the magnet focus, our mounting technique was changed, as shown in Figure 7, in imitation of the method used by ORTEC. In these units, epoxy is poured up to the level of the front surface of the silicon, and the gold is evaporated over the entire front surface to make its own contact to the grounded case. The signal lead is made to the rear surface of the silicon with conducting silver paint. The diode characteristics of three counters made in this fashion, using 900 Ω -cm n-type silicon, are shown in Figure 8. An alpha spectrum from a ThB source, taken with counter 9F and the biased amplifier as in Figure 2, is shown in Figure 9. Although a resolution of 120 keV is not outstanding for a solid-state detector, it is quite sufficient for this experiment.

The fast amplifiers shown in Figure 2 for the alpha channel are similar to those in the C^{12} channel, with the "variable delay," used to delay the alpha pulse by a time equal to the flight time of the C^{12} recoil ion, inserted between the first and second amplifiers. The delay consisted of from 0 to 255 feet of RG 114/U cable, which could be switch selected in increments of one foot. The signal velocity in this cable is 0.85 c; hence each foot of cable corresponds to a delay of 1.2 nsec.

The pulses from the alpha counter were higher than those from the C^{12} counter because the alpha energy was higher. Therefore less amplification was needed in the alpha channel in order to get the required pulse height for operation of the coincidence mixer. It was found that two of the Hewlett-Packard amplifiers could be replaced with type 460B's, which have lower gain but also have lower noise level. The output pulses were fed to the coincidence mixer and to the upper-beam input of the oscilloscope; the pulse height of an 8.5-MeV alpha particle was 1 volt (see the second highest group in Figure 5b). The scope gain used was 0.5 V/cm.

In place of a slow amplifier system such as used in the C^{12} channel, the alpha channel had a biased amplifier (see Figure 2). The 40-nsec-wide fast pulse was fed through an additional Hewlett-Packard type B amplifier to the biased amplifier which was set to discriminate against the high background of elastically scattered deuterons. The stretched and amplified pulse was then recorded on an RIDL 100-channel analyzer, so that gains could be monitored and scaler discriminator

biases set to count first-state (α_1) and ground-state (α_0) alpha particles.

E. Coincidence Detection

A tunnel-diode coincidence mixer was used in this experiment (see circuit diagram, Figure 10). Tunnel diodes were also used as discriminators at each input of the mixer. Input pulses of the order of half a volt were sufficient to trigger the diodes from the low-voltage to the high-voltage portion of the characteristic curve. This low-level switching characteristic was highly desirable because of the small pulses produced by solid-state counters; any additional gain in the fast C^{12} channel led to oscillation. The amplifiers included in the mixer produced a 20-V, 2- μ sec pulse for a count in either channel sufficient to switch the tunnel diode. These "fast C^{12} " and "fast α " pulses were counted and recorded as a monitor of the fast-amplifier gains and of the firing levels of the diodes. The coincidence output was a fast-rising pulse suitable for triggering the oscilloscope sweep.

Both the upper and lower beams of the oscilloscope were set to sweep on time base A, which was triggered by the coincidence mixer as shown in Figure 2. The sweep time was 0.1 μ sec/cm, and x5 magnification was used on both beams to give a resulting horizontal scale of 20 nsec/cm. During each sweep, a positive 20-V signal is provided at the "+ gate out" terminal of the time base unit. This pulse of 1- μ sec duration (0.1 μ sec/cm \times 10 cm) was counted on a scaler as the number of coincidences, and was also used as a gate signal for both of the multichannel analyzers. An additional output signal provided

by the oscilloscope is a "delayed trigger output," which was set to give a pulse at the end of the sweep time. This 8-V, 0.6- μ sec pulse was used to trigger the film-advance mechanism of the camera. As an aid to photography the regular P-2 green-phosphor cathode-ray tube was replaced by a CRT with a P-11 blue phosphor. The response of our film was much higher in the blue region of the spectrum. Also the P-11 phosphor has a higher brilliance and a much shorter persistence, which is important because our camera had no shutter. We were able to photograph persistent phosphorescence on the green tube for as much as half an hour after turning off an intense beam; no persistence of a quarter of a second or longer was observed with the P-11 phosphor.

It had originally been planned to observe the pulse-height spectrum from the counter at the magnet focus, gated by the coincidence mixer. However it soon became obvious that most of the C^{12} ions observed were in coincidence with first-state rather than second-state alphas, and furthermore that separation of C^{12} from B^{11} recoils (from $C^{13}(d, \alpha)B^{11}$ reactions) would be difficult. (See Figure 21c.) Thus it was necessary to obtain correlated coincidence spectra, and this was done in two ways. A simple but not always practical method was to write down the addresses from each multichannel analyzer as each coincidence occurred, the difficulty sometimes encountered being the "rapid" counting rate which averaged one count every five seconds. The other method was to photograph the dual-beam oscilloscope and to measure the pulse heights recorded on film. The dead time for this arrangement was only 1 μ sec per oscilloscope sweep, since double

exposures could be recorded while the film was in motion. The film gives as an additional piece of information the time separation of the two pulses. This was useful because it allowed us to decrease the time sensitivity of the coincidence mixer, and yet improve the time resolution of the experiment. Use of a two-dimensional multichannel analyzer, such as has since been acquired by the laboratory, would not have allowed this time measurement, and would not have had better energy resolution than the film system.

It might have been possible to use an existing camera and Polaroid film to take our photographs, but the retail cost of the film used would have been about \$6000. Furthermore the dead time involved in developing each print and changing film after every eight events would probably have more than doubled the running time of the experiment. Hence it was decided to design a camera to use film available in 100-foot rolls, and 35-mm film was chosen to obtain the largest practical negative size. Much assistance in choosing film and lens was received from Mr. Robert Macek and Dr. Hans Kobrak of the Synchrotron Laboratory. Tests with their cameras showed that an extremely fast lens was necessary to record single sweeps at 20 nsec/cm, and that Kodak Linagraph Pan film had better contrast and speed than either Tri-X or Royal-X Pan films. The fastest lens then available for 35-mm cameras, a Nikkor f/1.1, was obtained. The camera design is shown in Figure 11 and discussed more fully in Appendix B. A Beattie-Coleman electric film magazine was used; the circuit used to trigger the film-advance motor after each sweep

of the oscilloscope, shown in Figure 12, is also described in Appendix B, as is the film-developing procedure.

Not being designed for copy work, the lens was corrected only for distances greater than three feet. Thus when used at six inches, there was considerable barrel distortion, as can be seen in Figure 5a. However by using the same lens and the same geometry in an enlarger, all first order distortions were corrected. Figure 5b was printed in this manner from the same distorted negative as Figure 5a.

III. PROCEDURE AND RESULTS

A. Non-Coincident Recoil-Ion Spectra

For a magnetic spectrometer, the energy of a particle of mass M and charge Z is given by (Brown 1951):

$$E = C_m \frac{Z^2}{MI^2} \quad (11)$$

where C_m is a constant depending on the radius of the equilibrium orbit through the spectrometer, and I is the current reading of a torsion-balance fluxmeter (Lauritsen 1948). Thus an energy spectrum of the particles accepted by the magnet at a given current will show separate groups with different values of Z^2/M . Figure 13 is such a spectrum, taken with the alternating-gradient spectrometer at a setting $1/I^2 = 16.5$, corresponding to a proton energy of 1.85 MeV. In this spectrum two of the groups are recoil carbon ions: those with charge (4+) result from first-state events, and the higher energy (5+) group comes from ground-state events. Identification of the groups is aided by taking such spectra over a range of momentum (magnet) settings. Figure 14 is a contour plot of the energy spectra taken over the range $10.7 \leq 1/I^2 \leq 58.8$; counts are plotted vs. E and $1/I^2$. The 1/32-inch slit was used at the magnet image, and each spectrum was normalized to 20,000 ground- plus first-state alpha particles counted in the chamber detector.

B. Non-Coincident Alpha Spectra

The alpha-detection system was calibrated with a ThB source

(see Figure 9). A typical non-coincident alpha spectrum is shown in Figure 15. The four strong alpha groups above 5 MeV (bias is about 4 MeV for Figure 15) are identified by their energies as the three lowest states of the reaction $N^{14}(d,\alpha)C^{12}$, α_0 , α_1 , and α_2 respectively, and the ground state of $C^{13}(d,\alpha)B^{11}$. All the groups must be alpha particles because the counter bias was such that protons of 4 MeV or more would penetrate the depletion layer, resulting in pulses below the bias of the amplifier.

C. Procedure for Recording Coincidences

After positive identification of the various particle groups was made on the basis of the non-coincident spectra, the experimental procedure was as follows. First, the spectrometer current was varied and recoil-ion energy spectra were taken to find the maximum non-coincident counting rate of $C^{12}(4+)$ recoils from first-excited-state events. (See Figure 16. This figure and all others referred to in paragraphs C, D, and E of this section refer to that portion of the data which was taken on film #15.) All counting rates are normalized to the number $(\alpha_1 + \alpha_0)$ of first-state and ground-state alphas observed in the chamber counter, with the angle θ set to approximately the proper value. Then without changing the magnet current, the delay was adjusted so that coincident pulses observed on the dual-beam oscilloscope occurred at the same time; Figure 17 is a multiple exposure showing five $C^{12}(4+)-\alpha_1$ coincidences. Then the angle θ was varied to find the maximum coincidence counting rate for $C^{12}(4+)-\alpha_1$ events (see Figure 18). The maximum rate per 10,000 $(\alpha_1 + \alpha_0)$ is

called R_1 .

After thus optimizing, the three parameters were changed to the appropriate values for $C^{12}(3^+)-\alpha_2$ events.

$$\text{Fluxmeter: } I_2 = I_1 \times \sqrt{\frac{2.511}{1.706}} \times \frac{3}{4} = 0.910 I_1$$

$$\text{Delay: } \ell_2 = \ell_1 + 24 \text{ feet}$$

$$\text{Angle: } \theta_2 = \theta_1 - 3.7^\circ$$

The camera was connected, and runs of 40 μf on the charge integrator (or about 375 $\mu\text{coulomb}$ of beam) were made. As each coincidence occurred, the buzzer wired in parallel with the film-advance motor sounded, and an attempt was made to record the addresses from the 400-channel analyzer (recoil ion) and the 100-channel analyzer (biased alpha spectrum) on a line with the frame number of the picture.

These pulse heights were used to supplement the information on the film, and also served as a continuous check on gains and the overall performance of the system. The number of coincidences counted (number of sweeps of the oscilloscope) was also noted, in order to keep track of double and multiple exposures. Each sweep was recorded clearly even if the film was in motion; hence the dead time of the system was not determined by the half-second film-advance time, but only by the 1- μsec sweep time of the oscilloscope. At the end of each charge integration, the following numbers were recorded: elapsed time, number $(\alpha_1 + \alpha_0)$ of alphas of first-state energy and above (channel 30 and above in Figure 15), number α_0 of ground-state and higher alphas (channel 70 in Figure 15), number "fast α " of alpha singles sufficient to trigger the coincidence mixer, and number "fast C^{12} ,"

of particles in the recoil-ion channel energetic enough to trigger a coincidence. Thus a continuous check on the triggering levels for the coincidence mixer was made, as well as a check on target deterioration. Occasional photographs (such as Figure 5) of non-coincident spectra were taken as a check of gains and scope level shifts.

The results of a run are contained in three numbers:

$$R_1 = C^{12}(4+)-\alpha_1 \text{ coincidence rate per } 10,000 (\alpha_1 + \alpha_0);$$

$$\alpha = (\alpha_1 + \alpha_0)/10,000;$$

$$\text{Counts} = \text{number of } C^{12}(3+)-\alpha_2 \text{ events observed.}$$

D. Energy and Time Normalization

After films were developed, they were projected onto graph paper using the camera lens, and forming an image the same size as the original scope display. Each pulse height was estimated to 0.01 cm (probable error ± 0.03 cm), and the horizontal separation of the centroids of the two pulses was estimated to 0.1 cm (probable error ± 0.2 cm). The graph paper was adjusted so that the base line of the upper beam (alpha pulses) was on zero; correction was made in the normalization for the non-zero base line of the lower beam. At this stage noise and peculiar pulse shapes were rejected. Double exposures were also examined at this time; it was generally possible to correlate them properly by position on the film and by comparing pulse heights to observed multichannel analyzer addresses, if any, but occasionally two events were so overlapped that it was impossible to decide which upper-beam pulse belonged to which lower-beam pulse. These cases were discarded; in no case was a possible "real" $C^{12}(3+)-\alpha_2$

event involved. For identification purposes, the second event of a double exposure was given the negative of the frame number on which it occurred; all other events were identified by frame number. Of the 896 frames exposed on film #15, 45 were non-coincident calibrations, 11 extra sweeps were recorded from double exposures, and 349 frames were noise; thus 513 coincidences were recorded on film #15.

For each event, an IBM card was punched with the following six numbers: film and frame number, 100-channel address (alpha) if available, 400-channel address (recoil ion) if available, upper-beam pulse height (alpha) in cm, lower-beam pulse height (recoil ion) in cm, and horizontal separation (positive if lower beam displaced toward the right) in cm. The left half of Table III is an example showing the above information as punched on cards for frames 320 through 416 of film #15. Where no entry was punched for an analyzer address, an entry "-0." appears in Table III.

Since gains were adjusted each day, and subject to variation in any one day, the data were normalized in groups. The punched cards were fed to an IBM 7090 electronic data-processing machine in groups of between 30 and 300, depending on gain shifts or oscilloscope level shifts. The strongest coincident group was first-state alpha particles in coincidence with $C^{12}(3+)$ ions which had lost sufficient energy by straggling in the target to come through the magnet with the energy and velocity appropriate to second-state events. Because it was strongest, this group was used for calibration of all

three variables: both energies and the time. An estimate of the α_1 -pulse height on the upper beam was made, and the computer averaged all pulse heights within 10% of the estimate and set the result equal to 8.52 MeV. Assuming the oscilloscope pulse height proportional to energy, all upper-beam pulse heights were converted into energies (E UP in Table III). Also, a linear relation between the address of the 100-channel analyzer and the upper-beam pulse height was found by least squares, and the addresses were converted into energies (E100 in Table III). If no address was given, the energy E100 was set equal to E UP, but with a minus sign to indicate that it was not an independent measure of the energy.

The recoil-ion energy was normalized in the same manner, with the exception that the 400-channel analyzer address was the primary standard when it was available. This was done because of the poor resolution of the lower beam on the film resulting from the higher gain and higher noise level in the fast C^{12} channel as compared to the fast alpha channel. (Compare upper and lower-beam resolutions in Figure 17.) Thus the averages of all addresses within 10% of an estimated address for the $C^{12}(3+)$ ion was set equal to 1.706 MeV, and the address was assumed proportional to energy. Recoil-ion energies E LOW and E400 (see Table III) were calculated from the lower beam and from the 400-channel analyzer address when available; again $E400 = - E LOW$ if no address was recorded.

The time scale was normalized by averaging all values of the horizontal separation within 0.3 cm of the estimated separation of

the $C^{12}(3^+)-\alpha_1$ coincidences, and setting this average equal to $\Delta t = 0$. The horizontal scale factor was taken to be the oscilloscope setting of 20 nsec/cm, and a Δt was calculated for each event (DT in Table III).

E. Determination of the Number of Counts

After the normalization was completed, each event was added into the appropriate location in a $30 \times 27 \times 20$ array representing E UP, $|E400|$, and DT respectively. (The absolute value of E400 was taken because E400 had been given a negative sign if calculated from the lower beam instead of the 400-channel analyzer.) The range of alpha particle energy was from 4.625 to 12.125 MeV in 0.250 MeV steps; the range of recoil-ion energy was from 0.875 to 4.250 MeV in 0.125 MeV steps; and the range of Δt was from -52.5 to +47.5 nsec in 5.0 nsec steps, where $\Delta t = 0$ corresponds to a flight time of 162 nsec, and a negative Δt indicates a higher velocity ion. The three-dimensional array was printed out as 20 separate 27×30 two-dimensional arrays, each corresponding to a different value of Δt . The three center sections ($\Delta t = -5, 0, \text{ and } +5$ nsec) for the data from film #15 are reproduced as Figure 19 a, b, and c. The circled group is the $C^{12}(3^+)-\alpha_2$ group, and contains 26 counts. The entire three-dimensional array is plotted in isometric projection as a color-coded correlated coincidence spectrum in Figure 20.* Color is used to identify the vertical (time) axis, and a fourth dimension is provided by the area of the

* It is not practical to provide copies of Figure 20 in color with reproductions of the thesis. However either a duplicate 2 x 2-inch color slide or an 8 x 10-inch color print can be obtained at cost from the Kellogg Radiation Laboratory. In 1962, the cost of a duplicate slide was 30¢ and the cost of a print was \$3.50.

circle at each point, the area being proportional to the number of counts. The figure shows the $C^{12}(3+)-\alpha_2$ group well separated from all other groups, at $E_\alpha = 6.1$ MeV, $E_{C^{12}} = 1.7$ MeV, and $\Delta t = 0$ nsec.

The vertical columns along the left rear wall of the figure are deuterons in accidental coincidence with the various alpha-particle groups. For the α_0 and α_1 groups, they extend through all time from -40 to +40 nsec; for the less energetic alphas with smaller pulse heights, only deuterons within about 20 nsec registered as coincidences. Two other groups besides the group of interest occur at $\Delta t = 0$; the $C^{12}(3+)-\alpha_1$ group used for calibration, and also the $C^{13}(d,\alpha)B^{11}$ ground-state group, which is the closest neighbor to the group of interest (see Table I). At $\Delta t = -40$ nsec, higher energy $C^{12}(4+)$ ions straggled from ground-state events appear in coincidence with ground-state alphas. The remaining group at $\Delta t = -30$ nsec has mass 12 (from energy and velocity determinations), but an apparent charge of $3\frac{1}{2}$! This can be explained by recalling that first-excited-state events are 10^4 times as numerous as second-state events, and noting that the energies for the group are approximately those of the particles from a first-state reaction. Evidently the structure of the magnet is such that a (4+) ion can reach the center of the magnet, and if it undergoes a charge-exchanging collision there it may continue through the magnet as a (3+) ion. A collision probability of 1 in 10^4 within perhaps 4 cm of path length between the two segments of the magnet would be sufficient to produce the observed group. At a pressure of 10^{-6} mm Hg, this would correspond to a collision radius of 1.5 \AA .

To show that the visualization of the coincidence counting rate

as a function of three variables is necessary to identify counts, the data of film #15 are also presented as functions of the single variables Δt , E_{α} , and $E_{C^{12}}$ (see Figure 21). In each of this figure the solid areas are the 26 real counts identified from Figures 19 and 20, and the shaded areas are the accidental coincidences with elastically scattered deuterons in the recoil-ion channel. In Figure 21a these random coincidences provide a measure of the resolving time of the coincidence mixer. In Figure 21b the non-coincident alpha spectrum is reproduced (cf. Figure 15) by the accidental deuteron coincidences. Figure 21c confirms the statement made earlier that it is impossible to identify counts by observation of the coincident recoil-ion spectrum alone.

F. Experimental Results

After approximately 61 hours of running time with an average beam intensity of $1 \mu A$, the total number of counts obtained was 170. The total of non-coincident α_1 and α_0 was 4.01×10^7 . The value of R_1 , the $C^{12}(4+)-\alpha_1$ coincidence rate which was used as a measure of efficiency, varied with changes in target thickness, slit geometry, and possibly with vertical beam position; an approximate mean value for R_1 is 380, compared to the rate of $0.042 C^{12}(3+)-\alpha_2$ coincidences per 10,000 ($\alpha_1 + \alpha_0$). A summary of the data for individual runs is given in Table IV.

A background run was made using target C7-XIV, which had not been nitrated. It did contain about $0.05 \times 10^{17} N^{14}$ atoms/cm², however, which were probably included during the evaporation of vanadium, which is a good getter. The run lasted 5 hours (at $1-\mu A$ beam intensity),

which would have been sufficient to obtain 15 counts on an average target, or 0.2 counts from the nitrogen in the target used. No $C^{12}(3+)-\alpha_2$ counts were observed. The values of R_1 and α are included in Table IV.

IV. ANALYSIS OF RESULTS

A. Equation for $\Gamma_{\text{rad}}/\Gamma$

The ratio $\Gamma_{\text{rad}}/\Gamma$ is the ratio of the number of C^{12} surviving to the number of C^{12*} formed in the second excited state, or to the total number of α_2 produced in the reaction. If ϵ_2 is the efficiency of the system for detecting second-state coincidences,

$$\frac{\Gamma_{\text{rad}}}{\Gamma} = \frac{\text{observed } \text{C}^{12}(3+)-\alpha_2 \text{ coincidences}}{\epsilon_2 \times \text{total } \alpha_2} \quad (12)$$

The efficiency ϵ_1 for detecting first-state coincidences can be found directly by experiment, since for the first state we know that

$(\Gamma_{\text{rad}}/\Gamma)_1 = 1$; hence only the relative efficiency ϵ_2/ϵ_1 must be calculated.

$$\epsilon_1 = \frac{\text{observed } \text{C}^{12}(4+)-\alpha_1 \text{ coincidences}}{\text{total } \alpha_1} \quad (13)$$

$$\frac{\Gamma_{\text{rad}}}{\Gamma} = \frac{\text{Counts}/\alpha}{R_1} \times \frac{\epsilon_1}{\epsilon_2} \times \frac{\alpha_1}{\alpha_2} \quad (14)$$

Besides the relative population factor $P = \alpha_1/\alpha_2$ included explicitly in equation 14, the relative efficiency includes three correction factors. The most obvious, C, concerns the ratios of the various ionic-charge states of the recoiling nuclei, since we observe only a single charge state at a time. The second, G, has to do with differences in the effective solid angle for the two states, including the effects of deflections of the recoiling nuclei by gamma emission. The third correction, T, has to do with the momentum widths of the recoil-ion groups from the two states, compared to the 5% momentum window of the spectrometer.

$$\begin{aligned}
 \epsilon_2/\epsilon_1 &= C \times G \times T \\
 &= \frac{C^{12}(3+)/C^{12}(\text{total}) \text{ at } 1.71 \text{ MeV}}{C^{12}(4+)/C^{12}(\text{total}) \text{ at } 2.51 \text{ MeV}} \times \\
 &\quad \times \frac{\text{effective } d\Omega \text{ for second state}}{\text{effective } d\Omega \text{ for first state}} \times \\
 &\quad \times \frac{\% \text{ of } 2^{\text{nd}} \text{ state } C^{12} \text{ group in momentum window}}{\% \text{ of } 1^{\text{st}} \text{ state } C^{12} \text{ group in momentum window}} . \quad (15)
 \end{aligned}$$

Then

$$\frac{\Gamma_{\text{rad}}}{\Gamma} = \frac{\text{Counts}}{\alpha R_1} \times \frac{P}{CGT} ,$$

or $\frac{\Gamma_{\text{rad}}}{\Gamma} = \frac{\text{Counts}}{W} , \quad \text{where } W = \frac{CGT}{P} \times \alpha R_1 . \quad (16)$

Now the number W is proportional to the number of counts which would be obtained if there were no statistical fluctuations; thus the per cent statistical error for a given run is proportional to $1/\sqrt{W}$. If the result of each run is to be weighted inversely as the square of the error, the proper weighting factor is W . But

$$W \times \Gamma_{\text{rad}}/\Gamma = \text{Counts};$$

hence

$$\left(\frac{\Gamma_{\text{rad}}}{\Gamma} \right)_{\text{avg}} = \frac{\Sigma(\text{Counts})}{\Sigma(W)} . \quad (17)$$

Calculation of the various factors appearing in equation 16 and finally the calculation of $\Gamma_{\text{rad}}/\Gamma$ are given in the following sections.

B. Population Factor, P

From the alpha-particle spectrum of Figure 15, taken at the bombarding energy $E_d = 1.800$ MeV and the angle $\theta = 67^\circ$ used in the experiment, the factor P is

$$P = \alpha_1 / \alpha_2 = 3.00 \pm 0.09 . \quad (18)$$

P was measured at several energies and angles, and was found to be nearly constant between 1.7 and 1.9 MeV and between 67° and 71° . It is interesting to compare this result (equation 18) with the value $P = 17$ obtained by Hoyle (1953) and Dunbar (1953) at a bombarding energy of 672 keV and at a lab angle of 90° .

C. Charge-State Factor, C

To determine the charge-state ratios of carbon ions emerging from one of our VN targets, an elastic-scattering experiment was done. Alpha particles from the Office-of-Naval-Research tandem accelerator in Sloan Laboratory were used to bombard the carbon-foil backing of target C5-II (Table II), and C^{12} ions from $C^{12}(He^4, C^{12})He^4$ were observed emerging from the VN side of the target at a laboratory angle of $35\frac{1}{4}^\circ$. The recently installed 24-inch double-focusing magnetic spectrometer (Groce 1962) was used to analyze the emerging beam, and was varied to observe as many charge states as possible at each of three bombarding energies. The maximum solid angle (≈ 0.014 steradian) of the magnet was used, and the image slit was $\frac{1}{4}$ inch wide. The detector was a surface-barrier counter, and the energy spectra were recorded on a 400-channel analyzer. A single-channel discriminator

was set to include the C^{12} peak, which occurred at the same energy for each setting of the magnet. Another solid-state detector within the target chamber was set at about 90° and the elastically scattered alphas were used as a monitor of the charge integration and target deterioration.

At each of the three energies, which corresponded to ground-state, first-state, and second-state recoil energies from the $N^{14}(d,\alpha)C^{12}$ reaction, the magnet was set at the appropriate value to observe a prominent charge group, and the bombarding energy was varied to find the maximum counting rate. At the angle chosen, the C^{12} recoil has half of the energy of the incident particle; however because the ions pass through about half the carbon backing and all of the VN layer, the bombarding energies (given in Table V) had to be considerably higher. At each bombarding energy the magnet current was changed in proportion to $1/Z^2$ to observe the charge states Z.

Shown in Table V are the experimental results in the form of the C^{12} -counting rate divided by the alpha-counting rate in the chamber counter. Three or more readings were taken at each charge; the errors quoted in the table are either the spread of the readings or the statistical error, whichever was larger.

The data from Table V are converted into ratios in Table VI. The quoted errors were calculated as follows. Let the ratio corresponding to a charge state whose counting rate was A be

$$R = \frac{A}{A+B} ,$$

where B represents the sum of all other charge states besides A.

Then the square of the error in R is

$$\begin{aligned}
 (\delta R)^2 &= \left(\frac{\partial R}{\partial A} \delta A\right)^2 + \left(\frac{\partial R}{\partial B} \delta B\right)^2 \\
 &= \left(\frac{1}{A+B} \delta A - \frac{A}{(A+B)^2} \delta A\right)^2 + \left(-\frac{A}{(A+B)^2} \delta B\right)^2 \\
 &= \left(R \frac{\delta A}{A} - R^2 \frac{\delta A}{A}\right)^2 + \left(R \frac{B}{A+B} \frac{\delta B}{B}\right)^2 ; \\
 \left(\frac{\delta R}{R}\right)^2 &= (1 - R)^2 \left[\left(\frac{\delta A}{A}\right)^2 + \left(\frac{\delta B}{B}\right)^2\right] .
 \end{aligned} \tag{19}$$

It should be noted that the errors quoted in Table VI are purely statistical and do not include estimates of systematic error. Repetition of the experiment under more adverse conditions (instability of the magnetic-field-measuring device and rapid deterioration of the target) indicated that the errors should be doubled. The charge ratios from Table VI are plotted in Figure 22 as a function of the velocity of the ions.

The charge-ratio factor C is a ratio of two ratios. Though it is hoped that systematic errors should be reduced by taking ratios, the quoted errors in Table VI are doubled.

$$C = \frac{C^{12}(3+)/C^{12}(\text{total}) \text{ at } 1.71 \text{ MeV}}{C^{12}(4+)/C^{12}(\text{total}) \text{ at } 2.51 \text{ MeV}}$$

$$C = \frac{0.485 \pm 0.007}{0.341 \pm 0.007}$$

$$C = 1.421 \pm 2.5\% \tag{20}$$

D. Geometry Factor, G

The initial direction of a recoiling C^{12*} nucleus may be changed by gamma-ray emission. A first-state recoil at 90° has an energy of 2.511 MeV and a momentum of 237 MeV/c; emission of the 4.433-MeV γ -ray may deflect it by as much as 1.07° . Similarly the momentum of a second-state recoil is 195 MeV/c, and emission of two γ -rays with a total energy of 7.656 MeV will deflect the nucleus 2.25° if both γ -rays are in the same direction and at right angles to the path of the ion. In general, as many recoil ions will be deflected into the magnet entrance as are deflected away from it. However since the alpha-particle direction depends only on the initial direction of the recoil ion, an ion deflected into the magnet aperture may not be in coincidence with an observed alpha particle. The losses will be greater for the second state because of the greater possible deflection, and hence the relative efficiency will be affected.

Since both the spectrometer-entrance slit and the alpha-counter slit were tall compared to their widths, and the alpha slit was at least 2.8° taller than the spectrometer aperture, only the horizontal component of the deflection was considered. Figure 23 shows the notation used in the calculations. The center of the rectangular alpha slit, R, is at the angle θ_0 corresponding kinematically to C^{12*} recoils at 90° , and the angle θ is the angle determined by kinematics to correspond to a C^{12*} ion with an initial direction different from 90° by an amount δ . Momentum \vec{p}_γ is carried off by the emitted gamma or gammas, and the resulting deflection of the recoil ion is ψ , measured in the

horizontal plane. For small angles, the angle ψ is proportional to the component p_z of \vec{p}_γ parallel to the beam axis. Thus knowledge of the probability distribution for values of p_z determines the probability distribution for ψ .

The derivations of the probability functions $W_1(\psi)$ for the first state and $W_2(\psi)$ for the second state are given in Appendix C. If the emission of the 4.433-MeV γ -ray from the first state is isotropic, which we assumed to be the case, then the distribution $W_1(\psi)$ is rectangular (see Figure 24). The situation for the second state is more complicated. The first γ -ray, 3.223 MeV, is isotropic, but there is a strong angular correlation between the two E2 γ -rays. (From Figure 1 the level scheme is $0^+, 2^+, 0^+$.) If Θ is the angle between the two γ -rays (Frauenfelder 1955),

$$W(\cos \Theta) = 5/8 (1 - 3 \cos^2 \Theta + 4 \cos^4 \Theta) . \quad (21)$$

The z-component of the vector sum of the two γ -rays must be considered; the magnitude of the momentum \vec{p}_γ will vary between the sum (7.656 MeV/c) and the difference (1.210 MeV/c) of the two gammas with a probability distribution derived from equation 21. The final result for $W_2(\psi)$ is shown in Figure 24. Note that both curves in Figure 24 were calculated with $\delta = 0$; there will be a slight variation with δ because the initial momentum of the recoil ion is a function of δ .

The probability of detection as a function of δ and ψ depends upon the geometrical openings of the two slits, $R(\theta)$ for the rectangular slit and $E(\delta, \psi)$ for the elliptical aperture of the magnet. Since the

rectangular alpha slit is not located on the equator of the spherical co-ordinate system defined by the beam axis, its projection on the surface of the sphere is curved. The shape of a rectangle projected onto a sphere is derived in general in Appendix D, and drawn for two positions of the same slit in Figure 25. The pertinent value of θ_0 is 67.18° ; the shape at 10° is included only for contrast. Fortunately the elliptical slit is on the equator; its shape is given by the curve marked "ground state" in Figure 26.

Neglecting the vertical component of \vec{p}_γ , the recoil C^{12} and the α -particle are at the same inclination ϕ from the horizontal plane. Hence the minor of the two functions R and E ,

$$\Phi(\delta, \psi) = \min \{ R[\theta(\delta)] , E(\delta, \psi) \} \quad , \quad (22)$$

determines the probability that both the alpha and the C^{12} will be detected. (Account was also taken of the fact that the opening represented by the function $R(\theta)$ was not necessarily at $\phi = 0$.) The total effective solid angle for coincidence detection is

$$d\Omega = \int d\delta \int W(\psi) \Phi(\delta, \psi) d\psi \quad . \quad (23)$$

This expression was integrated numerically with an IBM 7090 computer for several different rectangular slits and for the two angular probability functions $W_1(\psi)$ and $W_2(\psi)$ given in Appendix C. The integral $I(\delta) = \int W(\psi) \Phi(\delta, \psi) d\psi$ for the slit 0.060 inch wide and 0.200 inch high is shown in Figure 26 for the first state and the second state. The curve for the ground state is just $\Phi(\delta, 0) = E(\delta)$. The asymmetry of

the second-state curve at -3° is due to the edge of the rectangular slit. The results of $d\Omega$ for the several cases are given in Table VII.

The geometrical correction factor G is the ratio of $d\Omega$ for the second state to $d\Omega$ for the first state. The probable error in the calculation of G was estimated on the assumption that the probable error of each calculated $d\Omega$ is 10% of the difference between $d\Omega$ and the maximum value, 0.0111 steradian. Values of G are also given in Table VII.

E. Thickness Factor, T

If all of the C^{12} ions entering the magnet aperture have momenta within the 5% resolution width of the magnet, they would presumably all be counted. As soon as the momentum width of the C^{12} group exceeds 5%, a correction must be applied to the counting efficiency. There is also a correction to the relative efficiency since the width of the group is a function of energy.

The first cause of width is target thickness. Using the mean square charge for C^{12} ions from Table VI, and proton stopping power data of Bader (1956) for V and Reynolds (1953) for N, the energy loss of C^{12} ions at the energies of interest in VN can be calculated from the relation that dE/dx will be Z^2 times dE/dx for protons of the same velocity. This is done in Table VIII. Also in Table VIII are the calculated energy losses at each of the three ion energies for the various targets used. This calculation was done assuming a VN layer with the number of molecules in it equal to the nitrogen content of the target as listed in Table II. The target is inclined at 60° to the

incident beam, so the number is divided by $\cos 30^\circ$.

Another source of momentum width is kinematic or $dE/d\theta$ broadening, including the extra width allowed by deflection of recoil ions into the magnet aperture by γ -emission. For the full width at half maximum of the energy spread from this cause, it is only necessary to measure the width of the curves of Figure 26. The values of $\Delta\delta$ and the corresponding ΔE_δ are entered in Table VIII. Actually the distributions in Figure 26 are functions of the rectangular slit used, but the full width at half maximum is virtually unaffected.

The final source of momentum broadening considered is the longitudinal component of the momentum of the emitted gamma rays. The probability distribution for a single component of the gamma momentum has already been calculated and is represented by the distributions $W(\psi)$ in Figure 24. The angle ψ (in radians) is the ratio of p_z/p ; p_z could just as well be the longitudinal component, and then $\Delta E_\gamma/E = 2 \Delta p/p = 2\psi$. The full width at half maximum $\Delta\psi$ and the corresponding ΔE_γ are also given in Table VIII.

The three energy spreads are summed in a simple fashion by taking the square root of the sum of the squares of the full widths at half maximum listed in Table VIII. The results, expressed as percent momentum widths, are listed in Table IX along with a few experimental measurements. The spectrometer resolution used to measure widths was 1.3% in momentum; see for instance Figure 16 which is a measurement of target C6-I, and Figure 14 for target C4-XI. It would not seem unreasonable to assign a probable error of 15% to the

calculated momentum widths.

The factor T required for the relative efficiency is the ratio of the per cent of the second-state group which is within the 5% momentum window of the spectrometer to the per cent of the first-state group within the window. These percentages are again calculated in a simple manner by assuming the group profile to be square with a width given by Table IX. Results and estimated errors for T are given in Table X. The error of the ratio is taken to be 25% of the amount of the correction, $1 - T$, combined with an additional 5% estimated systematic error, from comparing different calculations.

F. Calculation of $\Gamma_{\text{rad}}/\Gamma$

We now have measured or calculated all factors in equation 16. In Table XI the weighting factors W are calculated for each of the individual runs listed in Table IV. The data for each target are then treated as separate samples, and the values of $\Gamma_{\text{rad}}/\Gamma$ for each are calculated in Table XII and plotted in Figure 27. The mean value of $\Gamma_{\text{rad}}/\Gamma$ is also calculated, from equation 17.

The internal error is calculated from the statistical error of 170 counts and the standard deviation of ΣW , and the external error from the deviations of the five data groups from the mean. Combining the external error with an estimated 5% systematic error in the quantity T, the result of the experiment is

$$\frac{\Gamma_{\text{rad}}}{\Gamma} = (2.82 \pm 0.26) \times 10^{-4} \quad (24)$$

V. CONCLUSION

The result of this experiment is not significantly different from that of Alburger (1961), given in equation 6. Averaging our value with Alburger's, we obtain

$$\frac{\Gamma_{\text{rad}}}{\Gamma} = (2.9 \pm 0.3) \times 10^{-4} \quad (25)$$

Using the value for Γ discussed in section I B, $\Gamma = (8 \pm 5) \text{ eV}$, we obtain

$$\Gamma_{\text{rad}} = (0.0024 \pm 0.0015) \text{ eV} \quad (26)$$

This result is only a factor of $2\frac{1}{2}$ higher than that used by Salpeter (1957) in his energy-production-rate calculations. With our value for Γ_{rad} , equation 5 becomes

$$\epsilon = 3.3 \times 10^{21} \frac{\rho_5^2 x_\alpha^3}{T_8^3} f \exp\left(-\frac{43.2}{T_8}\right) \text{ erg/g sec.} \quad (27)$$

and the reaction rate for the formation of C^{12} is

$$P = 2.8 \times 10^{26} \frac{\rho_5^2 x_\alpha^3}{T_8^3} f \exp\left(-\frac{43.2}{T_8}\right) \text{ reactions/g sec.} \quad (28)$$

where ρ_5 is density in 10^5 g/cm^3 , x_α is the mass fraction of He^4 , T_8 is the temperature in $10^8 \text{ }^\circ\text{K}$, and f is the electron screening correction given approximately by (B² FH 1957)

$$f \approx \exp\left[0.88 \left(\frac{\rho_5}{T_8^3}\right)^{\frac{1}{2}}\right] \quad (29)$$

The mean lifetime for an alpha particle is given by

$$\frac{1}{\tau_{3\alpha}(\text{He}^4)} = \frac{3P}{n_\alpha} = 5.7 \times 10^3 \frac{(\rho_5 x_\alpha)^2}{T_8^3} f \exp\left(-\frac{43.2}{T_8}\right) \text{ sec}^{-1} . \quad (30)$$

This function, neglecting f , is represented by the curve labeled $3 \text{ He}^4 \rightarrow \text{C}^{12}$ in Figure 28, calculated for $\rho_5 x_\alpha = 1$. For comparison, the lifetime of a C^{12} nucleus in the reaction $\text{C}^{12}(\alpha, \gamma)\text{O}^{16}$ is also plotted. The latter rate depends on the unknown alpha width of a level at 7.12 MeV in O^{16} , just 40 keV below the $\text{C}^{12} + \alpha$ threshold. Fowler and Hoyle (1962) estimate $\theta_\alpha^2 = 0.78$ or 0.024, the former value being preferred theoretically and astronomically. With $\theta_\alpha^2 = 0.78$, the lifetime $\tau_\alpha(\text{C}^{12})$ for a C^{12} nucleus, in years, is given by

$$\begin{aligned} \log \tau_\alpha(\text{C}^{12}) = & -23.23 - \log \rho_5 x_\alpha + 2 \log T_8 \\ & + \frac{30.08}{T_8^{1/3}} + \frac{0.18}{T_8^{2/3}} , \end{aligned} \quad (31)$$

and if $\theta_\alpha^2 = 0.024$ the constant on the right becomes -21.72. Curves for both values of θ_α^2 are shown in Figure 28; the solid curve is for $\theta_\alpha^2 = 0.78$. An experiment by Larson and Spear now in progress in Sloan and Kellogg Laboratories may determine the $\text{C}^{12}(\alpha, \gamma)\text{O}^{16}$ rate more precisely.

Thus the rate of the 3α process as a function of density and temperature is now known to about 61%, the major source of uncertainty being the total width of the 7.656-MeV level in C^{12} . In this experiment, the ratio of the electromagnetic decay width to the total width was measured with a 9% probable error. In order to improve our knowledge of

Γ_{rad} , it would be necessary to increase the accuracy of the determination of Γ . A repetition of the inelastic-electron-scattering experiment to determine the absolute value of $\Gamma_{e\pm}$ might be called for. A reduction in the error assigned to the EO matrix element from 25% to 10% would provide a final result for Γ_{rad} with the error reduced to 40%. If the ratio $\Gamma_{e\pm}/\Gamma$ were also known to 20%, the total error in Γ_{rad} would be 30%.

APPENDIX A

Thin Nitrogen Targets

1. Carbon-foil backing

Microscope slides were cleaned thoroughly and then wet with glycerol. After the glycerol had been allowed to drain for an hour, the slides were placed in a vacuum system. A day was allowed to pump off the glycerol, and then carbon was sputtered onto the slides. To obtain a thick layer of carbon ($\sim 40 \mu\text{g}/\text{cm}^2$), sputtering was done in four fifteen-minute periods, with about fifteen minutes for cooling between each.

The carbon on the slides was divided into from ten to sixteen sections with a scribe, and the foils were floated off the slide in a shallow dish of distilled water two at a time. They were then lifted from the surface of the water on tantalum blanks which had a 1/4-inch or 5/16-inch hole. The foil had to cover the hole, and great care had to be taken to prevent wrinkles. Although it was easier to mount foils on clean blanks, it was found that the foils would adhere more permanently to blanks which had been lightly greased with vacuum grease.

2. Vanadium evaporation

Vanadium in wire or grain form was evaporated in vacuum from a tungsten boat. Because vanadium is an excellent getter, care was taken to shield the target blanks during the first melting of the vanadium. The pressure in the vacuum system was generally of the order of 10^{-6} mm Hg. About 20% of the foils were broken during evaporation. Instead of air, dry nitrogen gas was admitted to the

system after evaporation to try to prevent oxidation.

3. Nitriding

The nitriding procedure was to heat the target with an alpha-particle beam at the straight-through port of the 2-MeV Van de Graaff machine. Distilled ammonia was admitted to the chamber, as shown in Figure 3. The ammonia was first frozen (liquid N_2 temperature), and contaminants were pumped off. After being warmed and frozen three times, there was no change in the thermocouple-gauge reading when the (frozen) ammonia flask was opened to the system. Thus any oxygen was removed from the ammonia, but water was frozen with the ammonia. In order to keep water frozen during the nitriding, the ammonia flask was cooled to dry ice temperature, where the vapor pressure of NH_3 is 43 mm Hg and the vapor pressure of H_2O is 0.00055 mm Hg.

The pressure of NH_3 in the chamber during nitriding was of the order of 1 mm Hg. With the differential pumping and cold trap arrangement shown in Figure 3, no change was noted in the pressure in the accelerator column.

A beam of alpha particles (typically 0.8 μA at 700 keV) was used to heat the target to red heat, temperature being controlled by the needle valve controlling the ammonia pressure. The only analysis of the beam energy was done by the mass-separating magnet, but that deflected the beam enough to provide a signal for regulating the energy. The target was moved so that the entire central region was heated; ten minutes total nitriding time seemed to be sufficient to nitride a

target as completely as possible. About 20% of the foils were broken during nitriding.

4. Composition

Protons of 1 MeV were scattered from each target at the electrostatic-analyzer station of the 2-MeV Van de Graaff. Scattered particles were observed at a laboratory angle of 150° with the $10\frac{1}{2}$ -inch double-focusing spectrometer. Using the equation derived by Snyder (1950) for yield from a thin target in such a spectrometer, we have

$$\frac{nt}{\cos \theta_1} = \frac{2R_c}{\sigma q \Omega} \times 10^{15} \int \frac{N_q(I)}{I} d\alpha, \quad (A1)$$

where

nt = thickness of target in nuclei/cm²

θ_1 = angle between beam and target normal

R_c = resolution determined by slits at collector

σ = cross section of reaction = $4\pi \frac{d\sigma}{d\Omega}$

q = charge deposited

Ω = solid angle of spectrometer

$N_q(I)$ = number observed per charge q at fluxmeter setting I

From the concurrent work of Renken (1963),

$R_c = 307$

$\Omega = 1.47 \times 10^{-3}$ steradian

$q = 9.28 \mu\text{coulomb}$

Then for $\theta_1 = 15^\circ$, and $d\sigma/d\Omega$ in mbarns/steradian,

$$nt = 3.43 \times 10^{18} \times \frac{1}{\frac{d\sigma}{d\Omega}} \times \int \frac{N \rho(I)}{I} dI \quad (A2)$$

For the various elastic-scattering cross sections we used

C ¹² :	188 mb/ster	(Jackson 1953)
N ¹⁴ :	109 mb/ster	(Tautfest 1955)
O ¹⁶ :	154 mb/ster	(Eppling 1953)
V ⁵¹ :	787 mb/ster	(Rutherford 1911)

The scattering yield from a typical target is shown in Figure 4, and the calculated compositions for the various targets used are given in Table II.

APPENDIX B

Camera and Film Developing

The optical properties of the Nikkor f/1.1 lens were measured on an optical bench. The focal point F in object space was found to be 0.172 inch in front of the frontmost metal ring, the focal point F' in image space is 0.825 inch behind the rearmost metal piece, and the focal length was measured as 2.03 inches. The locations of the foci F and F' and the corresponding principal planes H and H' are shown in Figure 11, referred to the rear surface of the mounting ring. This stainless steel ring, 0.349 inch thick, has six 4-40 clearance holes on a 2.200-inch circle, and could be used to mount the lens to other equipment. The dimensions given correspond to a range setting on the lens of six feet; there is travel 0.064 inch either way from this position.

For a magnification of $1/3$, the film plane had to be $\frac{1}{3} \times f = 0.68$ inch behind the plane F' , as shown in Figure 11. The range over which the camera can be focused in this configuration is approximately one inch. If the spacer ring in Figure 11 is removed, the distance settings on the lens should approximately correspond to actual focus.

The film magazine has an electric motor and a microswitch which is operated by a cam turned by the moving film. If power is supplied to the motor long enough to move the cam far enough to throw the switch, the switch will then keep the motor on until the film has advanced one frame. A circuit using a silicon controlled rectifier (SCR) and a relay to start the film advance when triggered by a short pulse is shown in Figure 12. A buzzer and two neon lights are wired in

parallel with the film-advance motor to warn the operator. Each advance is also counted on a mechanical register in the power supply unit.

The film used was Kodak Linagraph Pan, LP417 in 100-foot rolls. It was developed in a Morse G-3 rewind tank, using D-8 developer, as follows:

1. Prebath, Kodak "Photoflo," 2 min.
2. Develop, D-8, 68 °F, 9 min.
3. Stop, 1% HAc, 2 min.
4. Rinse, running water, 2 min.
5. Fix, fr "Rapid Fixol" + liquid hardener, 6 min.
6. Rinse, running water, 2 min.
7. Clear, Kodak "Hypo Clearing Agent," 2 min.
8. Wash, running water, 6 min.
9. Photoflo, 2 min.
10. Dry.

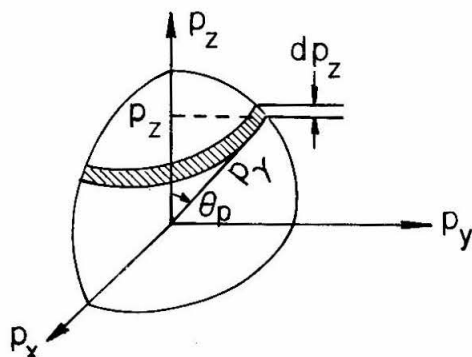
Because the lens was used so close to the object, a serious barrel distortion was introduced, as shown in Figure 5a. Therefore an enlarger was constructed using the camera base plate and lens, and modifying a Beattie-Coleman ground glass holder for use as a film guide. Note that it is disastrous to use a bulb with too high wattage, since the cement used in the lens is subject to melting. In this case a 50-watt bulb was used, but it was run at about 60 V instead of 110 V. Figure 5b is a print made using this arrangement.

APPENDIX C

Momentum of Gamma Rays

1. First excited state

The first excited state of C^{12} decays by emission of a 4.433-MeV γ -ray, adding a vector momentum \vec{p}_γ with magnitude 4.433 MeV/c to the recoiling nucleus. (See Figure 23.) Let p_z be a single component of the γ -ray momentum vector \vec{p}_γ , and let $W(p_z)dp_z$ be the probability that the value of the component lies between p_z and $p_z + dp_z$. Assuming \vec{p}_γ isotropic, $W(p_z)dp_z$ is just the fraction of the surface of the sphere in momentum space of radius p_γ between



the planes p_z and $p_z + dp_z$.

$$W(p_z)dp_z = \frac{1}{4\pi p_\gamma^2} \times 2\pi(p_\gamma \sin \theta_p) \times \frac{dp_z}{\sin \theta_p} \quad (C1)$$

$$W(p_z)dp_z = \begin{cases} \frac{1}{2p_\gamma} dp_z, & p_z^2 < p_\gamma^2 \\ 0, & p_z^2 > p_\gamma^2. \end{cases} \quad (C2)$$

Since the angle of deflection of the recoil nucleus is small, its projection in the horizontal plane is just $\psi = p_z/p_1$, where p_1 is the initial magnitude

of the momentum of the recoil nucleus. Then

$$p_z = p_1 \psi$$

$$W_1(\psi)d\psi = W[p_z(\psi)] dp_z(\psi) = \frac{1}{2p_\gamma} \times p_1 d\psi$$

$$W_1(\psi)d\psi = \begin{cases} \frac{p_1}{2p_\gamma} d\psi, & |\psi| < p_\gamma/p_1 \\ 0 & |\psi| > p_\gamma/p_1 \end{cases} \quad (C3)$$

Note that $W_1(\psi)$ given by equation C3 is a function of p_1 and hence of the angle δ . $W_1(\psi)$ for $\delta = 0$ is plotted in Figure 24.

2. Second excited state

The (0+) second state of C^{12} decays by E2-E2 γ -cascade through the (2+) first state to the (0+) ground state. If Θ is the angle between the two γ -rays, the angular correlation is

$$W(\mu)d\mu = 5/8(1-3\mu^2 + 4\mu^4)d\mu, \text{ where } \mu = \cos \Theta. \quad (C4)$$

In this case the magnitude p_γ of the γ -momentum is not a constant, but will have a probability distribution $W(p_\gamma)dp_\gamma$, and equation C3 will have to be integrated over all possible values of p_γ :

$$W_2(\psi)d\psi = \frac{p_2}{2} d\psi \int_{p_2|\psi|}^{p_{\max}} \frac{W(p_\gamma)}{p_\gamma} dp_\gamma, \quad (C5)$$

where p_2 is the initial recoil-ion momentum, and the lower limit of the integration results from the limit in equation C3.

The magnitude p_γ is given by the law of cosines:

$$p_Y^2 = p_{3.2}^2 + p_{4.4}^2 + 2 p_{3.2} p_{4.4} \cos \theta, \text{ or}$$

$$p_Y^2 = a^2 + b^2 \mu \tag{C6}$$

where $a^2 = 30.039 \text{ MeV}^2/c^2$ and $b^2 = 28.575 \text{ MeV}^2/c^2$.

Thus

$$\mu = \frac{1}{b^2} (p_Y^2 - a^2) \tag{C7}$$

$$d\mu = \frac{1}{b^2} (2p_Y) dp_Y. \tag{C8}$$

Having expressed μ as a function of p_Y , we can state

$$W(p_Y) dp_Y = W[\mu(p_Y)] d\mu(p_Y) = W(\mu) \frac{d\mu}{dp_Y} dp_Y$$

$$W(p_Y) dp_Y = 5/8 [1 - 3 \frac{1}{b^4} (p_Y^2 - a^2)^2 + 4 \frac{1}{b^8} (p_Y^2 - a^2)^4] \frac{2p_Y}{b^2} dp_Y. \tag{C9}$$

There are a maximum and a minimum value for p_Y :

$$p_{\max} = p_{3.2} + p_{4.4} = (a^2 + b^2)^{\frac{1}{2}} = 7.656 \text{ MeV}/c$$

$$p_{\min} = |p_{3.2} - p_{4.4}| = (a^2 - b^2)^{\frac{1}{2}} = 1.210 \text{ MeV}/c; \tag{C10}$$

the value of $W(p_Y) dp_Y$ is zero outside these limits. Note that

$$\int_{p_{\min}}^{p_{\max}} W(p_Y) dp_Y = 1.$$

Letting $F(p_Y) = \int \frac{W(p_Y)}{p_Y} dp_Y$, we have from equation C5

$$W_2(\psi)d\psi = \begin{cases} 0, & |\psi| > p_{\max}/p_2 \\ \frac{p_2}{2} [F(p_{\max}) - F(p_2 |\psi|)] d\psi, & \frac{p_{\min}}{p_2} \leq |\psi| \leq \frac{p_{\max}}{p_2} \\ W_2 \left(\frac{p_{\min}}{p_2} \right) d\psi, & |\psi| < p_{\min}/p_2 \end{cases} \quad (C11)$$

and

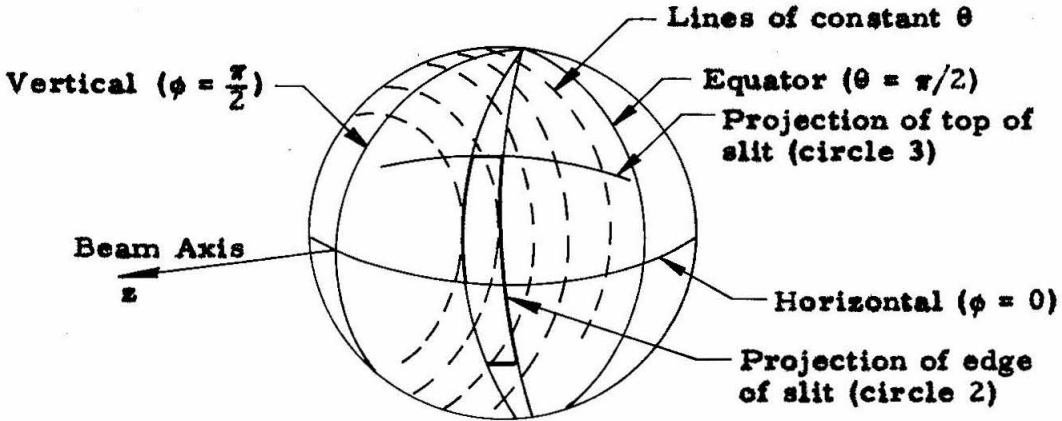
$$F(p_Y) = \frac{5}{4b^2} \left[\left(1 - 3 \frac{a^4}{b^4} + 4 \frac{a^8}{b^8} \right) p_Y + \frac{1}{3} \left(6 \frac{a^2}{b^4} - 16 \frac{a^6}{b^8} \right) p_Y^3 \right. \\ \left. + \frac{1}{5} \left(-\frac{3}{b^4} + 24 \frac{a^4}{b^8} \right) p_Y^5 - \frac{16}{7} \frac{a^2}{b^8} p_Y^7 + \frac{4}{9} \frac{1}{b^8} p_Y^9 \right]. \quad (C12)$$

Like the equation C3, the distribution C11 is also a function of the angle δ (see Figure 23) through the recoil-ion momentum p_2 . It is plotted in Figure 24 for $\delta = 0$. The calculation was done on the IBM 7090 as a part of the calculation of G.

APPENDIX D

Projection of a Rectangle in Spherical Co-ordinates

A rectangular slit, such as used to define the solid angle of the alpha counter in this experiment, does not present a rectangular opening in (ϕ, θ) space; the farther the slit is from the "equator" ($\theta = \pi/2$), the more curved the projection will be, with the extremities pointed toward the equator. Also, if the slit is not short compared to its distance from the center of the sphere, the ends will subtend a smaller angle than the central portion.



We shall make use of the properties of a right spherical triangle. If a , b , and c are three intersecting great-circle arcs, and A , B , and C are the angles opposite the sides a , b , and c , and if angle $C = \pi/2$, then

$$\sin a = \sin A \sin c \tag{D1}$$

$$= \tan b \cot B \tag{D2}$$

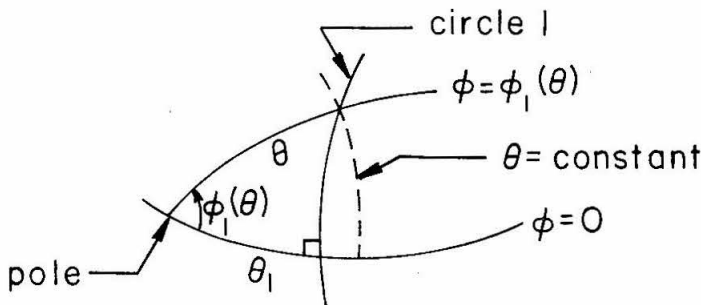
$$\cos A = \cos a \sin B \tag{D3}$$

$$= \tan b \cot c \tag{D4}$$

$$\cos c = \cot A \cot B \tag{D5}$$

$$= \cos a \cos b \tag{D6}$$

Take the slit to be of width w , height h , centered at $\theta = \theta_0$ and $\phi = 0$, and at a distance r from the center of the sphere. We consider only the quadrant $0 < \theta \leq \pi/2$; the pole cannot be included without added complications. The vertical line forming either edge of the slit will project onto the sphere as a great circle perpendicular to the horizontal ($\phi = 0$) circle. Let $\theta_1 = \theta_0 - \text{atan}(w/2r)$ be the value of θ at which the edge nearest the pole intersects $\phi = 0$, and call its projection circle 1. Every latitude circle with $\theta \geq \theta_1$ will intersect circle 1; let the value of ϕ at the intersection be $\phi_1(\theta)$. Then arcs of $\phi = 0$, $\phi = \phi_1(\theta)$, and circle 1 form a right spherical triangle. The length of the $\phi = 0$ arc is θ_1 , and the length of the $\phi = \phi_1(\theta)$ arc is θ ; the angle



between these two arcs is $\phi_1(\theta)$. From equation D4,

$$\cos \phi_1(\theta) = \tan \theta_1 \cot \theta \tag{D7}$$

Similarly for the other edge of the slit, let $\theta_2 = \theta_0 + \text{atan}(w/2r)$ be the

Any latitude circle $\theta > \theta_3$ will intersect circle 3 in two places. However one of these will be at an angle greater than α and hence greater than $\pi/2$; it has no significance unless the slit is wide enough to include the pole. Let $\phi_3(\theta)$ be the co-ordinate of the intersection less than α . Then from the right spherical triangle formed by $\phi = \phi_3(\theta)$, $\phi = \alpha$, and circle 3, with respective arc lengths θ , θ_3 , and unknown, using equation D4,

$$\cos[\alpha - \phi_3(\theta)] = \tan \theta_3 \cot \theta \quad . \quad (D11)$$

To summarize, the calculation proceeded as follows. Given θ_0 , h , w , and r , we have

$$\theta_1 = \theta_0 - \text{atan}(w/2r), \quad (D12a)$$

$$\theta_2 = \theta_0 + \text{atan}(w/2r), \quad (D12b)$$

$$\phi_0 = \text{atan}(h/2r), \quad (D12c)$$

$$\theta_3 = \text{asin}(\sin \phi_0 \cos \theta_0), \quad (D12d)$$

$$\alpha = \text{acos}(-\tan \theta_3 \tan \theta_0). \quad (D12e)$$

These parameters describe the size of the slit and its position. As functions of polar angle θ , the equations $\phi(\theta)$ for the sides and top of the slit are:

$$\phi_1(\theta) = \begin{cases} \text{acos}(\tan \theta_1 \cot \theta), & \theta > \theta_1 \\ 0, & \theta \leq \theta_1 \end{cases} \quad (D13)$$

$$\phi_2(\theta) = \begin{cases} \alpha \cos (\tan \theta_2 \cot \theta), & \theta > \theta_2 \\ 0, & \theta \leq \theta_2 \end{cases} \quad (D14)$$

$$\phi_3(\theta) = \begin{cases} \alpha - \alpha \cos (\tan \theta_3 \cot \theta), & \theta \geq \theta_3 \\ \pi, & \theta < \theta_3 \end{cases} \quad (D15)$$

The values of ϕ outside the limits of θ within which they were derived are defined as above for convenience.

The maximum value of ϕ which is within the slit opening at a given θ is either $\phi_1(\theta)$ or $\phi_3(\theta)$, whichever is smaller; the lower limit (non-negative) ϕ is $\phi_2(\theta)$. Thus the $\Delta\phi$ opening of the slit as a function of θ is $R(\theta)$, given by

$$\frac{1}{2}R(\theta) = \min [\phi_1(\theta), \phi_3(\theta)] - \phi_2(\theta) \quad (D16)$$

The solid angle of the slit is

$$d\Omega = \int_0^{\pi/2} R(\theta) \sin \theta \, d\theta \quad (D17)$$

The shape of a slit used in the experiment ($h = 0.200$ inch, $w = 0.060$ inch, $r = 0.625$ inch) is shown in Figure 25. It was used at $\theta_0 = 67.18^\circ$; it was also calculated at $\theta_0 = 10^\circ$ for contrast. The solid angle $d\Omega$ was 0.0303 steradians, independent of position.

REFERENCES

- F. Ajzenberg-Selove and T. Lauritsen, 1959, *Nuclear Physics* 11, 1.
(See Figure 1.)
- F. Ajzenberg-Selove and P. H. Stelson, 1960, *Phys. Rev.* 120, 500.
(See text pp. 3, 4.)
- D. E. Alburger, 1960, *Phys. Rev.* 118, 235. (See text pp. 3, 4.)
- D. E. Alburger, 1961, *Phys. Rev.* 124, 193. (See text pp. 4, 37.)
- M. Bader, R. E. Pixley, F. S. Mozer, and W. Whaling, 1956, *Phys. Rev.* 103, 32. (See text p. 34.)
- A. B. Brown, C. W. Snyder, W. A. Fowler, and C. C. Lauritsen, 1951, *Phys. Rev.* 82, 159. (See text p. 16.)
- $B^{27}\text{FH}$: E. M. Burbidge, G. R. Burbidge, W. A. Fowler, and F. Hoyle, 1957, *Revs. Modern Phys.* 29, 547. (See text pp. 3, 37.)
- C. W. Cook, W. A. Fowler, C. C. Lauritsen, and T. Lauritsen, 1957, *Phys. Rev.* 107, 508. (See text pp. 1-3.)
- G. Dearnaley and A. B. Whitehead, 1961, *Nucl. Instr. and Meth.* 12, 205. (See text p. 10.)
- D. N. F. Dunbar, R. E. Pixley, W. A. Wenzel, and W. Whaling, 1953, *Phys. Rev.* 92, 649. (See text pp. 1, 5, 28.)
- S. F. Eccles and D. Bodansky, 1959, *Phys. Rev.* 113, 608. (See text p. 3.)
- F. J. Eppling, J. R. Cameron, R. H. Davis, A. S. Divatia, A. I. Galonsky, E. Goldberg, and R. W. Hill, 1953, *Phys. Rev.* 91, 438A; also F. J. Eppling, Thesis, 1953, University of Wisconsin. (See Appendix A, p. 43.)

- Everling, König, Mattauch, and Wapstra, 1960, *Nuclear Physics* 15, 342. (See text p. 2.)
- W. A. Fowler and F. Hoyle, 1962, "Neutrino Processes in Supervovae," to be published. Also W. A. Fowler, private communication. (See text, p. 38.)
- H. Frauenfelder, 1955, Beta- and Gamma-Ray Spectroscopy, K. Siegbahn, ed., p. 556 (North-Holland Publishing Co., Amsterdam). (See text p. 32, Appendix C, p. 47.)
- J. H. Fregeau, 1956, *Phys. Rev.* 104, 225. (See text p. 4.)
- Gmelins Handbuch der Anorganischen Chemie, 1936, 8 Auflage, Nummer 36, s. 71. (Verlag Chemie, G. m. b. H., Berlin, 1936.) (See text p. 7.)
- D. E. Groce, J. H. McNally, and W. Whaling, 1962, *Bull. Am. Phys. Soc.* 7, 453. (See text p. 28.)
- A. Hemmendinger, 1948, *Phys. Rev.* 73, 806; *Phys. Rev.* 75, 1267 (1949). (See text p. 1.)
- F. Hoyle, D. N. F. Dunbar, W. A. Wenzel, and W. Whaling, 1953, *Phys. Rev.* 92, 1095. (See text pp. 1, 5, 28.)
- F. Hoyle, 1954, *Astrophys. J. Suppl.* 1, 121. (See text p. 1.)
- H. L. Jackson, A. I. Galonsky, F. J. Eppling, R. W. Hill, E. Goldberg, and J. R. Cameron, 1953, *Phys. Rev.* 89, 365. (See Appendix A, p. 43.)
- R. W. Kavanagh, 1958, *Bull. Am. Phys. Soc.* 3, 316. (See text p. 3.)
- C. C. Lauritsen and T. Lauritsen, 1948, *Rev. Sci. Instr.* 19, 916. (See text p. 16.)

- T. Lauritsen and F. Ajzenberg-Selove, 1962, "Energy Levels of Light Nuclei," Nuclear Data Sheets, 1961, Sets 5 and 6. (See Figure 1.)
- H. J. Martin and A. A. Kraus, 1957, *Rev. Sci. Instr.* 28, 175; also H. J. Martin, thesis, California Institute of Technology, 1956. (See text p. 7.)
- E. J. Öpik, 1951, *Proc. Roy. Irish Acad.* A54, 49. (See text p. 1.)
- E. J. Öpik, 1953, *Mem. Soc. Roy. Sci. Liège* 14, 131. (See text p. 1.)
- J. R. Oppenheimer and J. S. Schwinger, 1939, *Phys. Rev.* 56, 1066. (See text p. 4.)
- J. H. Renken, 1963, Thesis, California Institute of Technology (unpublished). (See Appendix A, p. 42.)
- H. K. Reynolds, D. N. F. Dunbar, W. A. Wenzel, and W. Whaling, 1953, *Phys. Rev.* 92, 742. (See text p. 34.)
- E. Rutherford, 1911, *Phil. Mag.* 21, 669. (See Appendix A.)
- E. E. Salpeter, 1952, *Ap. J.* 115, 326; Annual Reviews of Nuclear Science (Annual Reviews, Inc., Stanford, 1953), Vol. 2, p. 41. (See text p. 1.)
- E. E. Salpeter, 1954, *Australian J. Phys.* 7, 373. (See text p. 3.)
- E. E. Salpeter, 1957, *Phys. Rev.* 107, 516. (See text pp. 1, 2, 37.)
- L. I. Schiff, 1955, *Phys. Rev.* 98, 1281. (See text p. 4.)
- R. J. Sime and J. L. Margrave, 1956, *J. Phys. Chem.* 60, 810. (See text p. 7.)
- C. W. Snyder, S. Rubin, W. A. Fowler, and C. C. Lauritsen, 1950, *Rev. Sci. Instr.* 21, 852. (See Appendix A.)

G. W. Tautfest, J. R. Havill, and S. Rubin, 1955, Phys. Rev. 98,
280A. (See Appendix A, p. 43.)

A.V. Tollestrup, W. A. Fowler, and C. C. Lauritsen, 1949, Phys.
Rev. 76, 428. (See text p. 1.)

Table I
Kinematics of $N^{14}(d,\alpha)C^{12}$

For a deuteron energy of 1.800 MeV, the relativistically correct energies of C^{12} ions at 90° in the lab, the corresponding α energies, the lab angle θ of the α 's, and the flight time t of the C^{12} ions through 85 cm are given. The ground state of the reaction $C^{13}(d,\alpha)B^{11}$ is also included. (See text pp. 6, 23.)

State	ion energy	α energy	θ	t
C^{12} ground	3.620 MeV	11.759 MeV	73.9°	111 nsec
C^{12*} (4.433 MeV)	2.511	8.435	70.9	134
C^{12*} (7.656 MeV)	1.706	6.017	67.2	162
B^{11} ground	1.616	5.351	65.8	160

Table II

Target Composition

Compositions of various targets in units of 10^{17} atoms/cm² calculated as in Appendix A from yield curves similar to Figure 4. (See text p. 7.)

Target	C ¹²	N ¹⁴	O ¹⁶	V ⁵¹
C4-XI	22.4	2.6	0.2	3.1
C5-I	15.6	0.3	0.1	0.4
C5-II	14.5	0.7	0.3	0.8
C6-I	16.6	1.4	0.1	1.3
C6-VIII	19.1	3.3	0.5	4.0
C6-IX	19.6	2.8	0.5	4.3
C6-XII	22.1	3.1	0.4	4.9
C7-XVI	22.4	1.2	0.3	1.3

Table III

Input Data and Calculated Normalization

The first column gives the identification (film and frame) number of each event; the data presented here are frames 320 through 416 of film #15, and frame 336 is a double exposure. The next five columns are the input data: 100 channel address, 400 channel address, upper-beam pulse height in cm, lower-beam pulse height in cm, and horizontal separation (positive if lower-beam pulse is to the right) in cm. The final five columns are the energy and time equivalents of the five data columns. E100 and E UP refer to the alpha-particle energy in MeV, and E400 and E LOW to the C^{12} recoil-ion energy in MeV. DT is the time separation (difference from 162 nsec) in nsec. Five frames included in this table represent $C^{12}(3+)-\alpha_2$ events; they are 338, 356, 362, 373, and 405. (See text pp. 20-22.)

TABLE III

NUMBER	DATA					CALCULATED				
	CH1	CH4	CMUP	CMLC	CMCT	E100	E400	E UP	E LOW	DT
15320	-C.	63.	0.90	1.70	C.9	-3.55	2.45	3.55	2.47	14.
15321	24.	71.	1.90	0.90	C.5	7.91	2.76	8.43	1.04	6.
15327	7.	38.	1.71	1.21	C.5	5.70	1.48	5.37	1.60	6.
15328	-C.	-0.	1.91	1.00	-C.7	-8.48	-1.22	8.48	1.22	-18.
15329	52.	30.	2.52	0.87	C.9	11.55	1.17	11.18	0.99	14.
15330	-C.	-0.	2.58	2.30	-1.7	-11.45	-3.54	11.45	3.54	-38.
15331	-C.	-0.	2.72	2.31	-C.	-9.85	-3.56	9.85	3.56	-4.
15334	5.	36.	1.70	1.26	C.5	5.44	1.40	5.33	1.69	6.
15336	-C.	-0.	1.70	0.90	-C.2	-5.77	-1.04	5.77	1.04	-8.
-15336	7.	36.	1.76	1.10	-C.	5.70	1.40	6.04	1.40	-4.
15338	7.	44.	1.76	1.35	C.2	5.70	1.71	6.04	1.85	0.
15341	5.	33.	1.16	1.07	-C.2	5.44	1.28	5.15	1.35	-8.
15342	8.	43.	1.73	1.20	C.1	5.83	1.67	5.46	1.58	-2.
15343	51.	32.	2.60	0.90	-C.3	11.42	1.24	11.54	1.04	-10.
15345	-C.	35.	2.54	0.87	C.4	-11.27	1.36	11.27	0.99	4.
15346	22.	43.	1.91	1.40	C.2	7.65	1.67	8.48	1.94	0.
15347	23.	46.	1.90	1.47	C.2	7.78	1.79	8.43	2.06	0.
15348	10.	32.	1.49	0.94	-C.2	6.09	1.24	6.61	1.12	-8.
15349	30.	33.	1.98	1.00	-C.6	8.69	1.28	8.79	1.22	-16.
15350	53.	33.	2.53	0.80	-C.1	11.68	1.28	11.23	0.87	-6.
15352	29.	31.	1.90	1.00	C.2	8.56	1.20	8.43	1.22	0.
15353	28.	42.	1.91	1.25	C.3	8.43	1.63	8.48	1.67	2.
15354	10.	29.	1.78	1.00	1.0	6.09	1.13	6.12	1.22	16.
15356	10.	48.	1.42	1.62	C.1	6.09	1.87	6.30	2.33	-2.
15357	-C.	31.	1.71	1.04	C.3	-5.37	1.20	5.37	1.29	2.
15359	30.	31.	1.91	0.93	C.4	8.69	1.20	8.48	1.10	4.
15361	31.	31.	1.93	0.54	-C.7	8.82	1.20	8.56	1.12	-18.
15362	12.	47.	1.42	1.37	C.1	6.35	1.83	6.30	1.88	-2.
15363	28.	28.	1.90	1.08	1.3	8.43	1.09	8.43	1.37	22.
15364	7.	31.	1.70	1.00	-1.1	5.70	1.20	5.33	1.22	-26.
15365	27.	68.	1.91	1.91	-1.2	8.30	2.64	8.48	2.85	-28.
15367	28.	32.	1.91	1.10	1.0	8.43	1.24	8.48	1.40	16.
15368	53.	28.	2.71	0.87	C.7	11.68	1.09	11.58	0.99	10.
15369	7.	39.	1.77	1.11	C.5	5.70	1.52	5.64	1.42	6.
15370	51.	32.	2.50	0.83	C.9	11.42	1.24	11.09	0.92	14.
15373	9.	46.	1.79	1.48	C.1	5.96	1.79	6.17	2.08	-2.
15374	11.	32.	1.76	1.00	-1.3	6.22	1.24	6.04	1.22	-30.
15375	20.	54.	1.73	1.66	-C.1	7.39	2.10	7.68	2.40	-6.
15376	29.	32.	1.98	0.90	-1.0	8.56	1.24	8.34	1.04	-24.
15377	51.	33.	2.56	1.00	-1.3	11.42	1.28	11.36	1.22	-30.
15378	12.	30.	1.40	0.85	C.3	6.35	1.17	6.21	0.96	2.
15379	9.	33.	1.71	1.12	-C.2	5.96	1.28	5.81	1.44	-8.
15381	27.	46.	1.93	1.53	C.2	8.30	1.79	8.56	2.17	0.
15384	27.	31.	1.97	1.00	-1.1	8.30	1.20	8.74	1.22	-26.
15385	33.	31.	2.70	1.00	-1.1	9.08	1.20	8.88	1.22	-26.
15388	49.	32.	2.58	0.90	C.3	11.16	1.24	11.45	1.04	2.
15389	30.	30.	1.95	1.00	-C.4	8.69	1.17	8.65	1.22	-12.
15390	33.	30.	2.76	0.90	-C.1	9.08	1.17	9.14	1.04	-6.
15392	6.	39.	1.70	1.36	C.3	5.57	1.52	5.33	1.86	2.
15393	-C.	31.	1.92	1.00	-1.3	-8.52	1.20	8.52	1.22	-30.
15397	-C.	-0.	1.93	0.90	-C.8	-8.56	-1.04	8.56	1.04	-20.
15400	50.	32.	2.50	0.85	C.6	11.29	1.24	11.09	0.96	8.
15401	-C.	33.	1.92	0.87	-C.6	-8.52	1.28	8.52	0.99	-16.
15403	28.	33.	1.90	1.22	C.4	8.43	1.28	8.43	1.61	4.
15405	11.	42.	1.42	1.41	C.3	6.22	1.63	6.30	1.95	2.
15406	27.	57.	1.91	0.90	C.3	8.30	2.21	8.48	1.04	2.
15407	11.	66.	1.44	1.90	-C.5	6.22	2.56	6.39	2.83	-14.
15408	29.	29.	1.91	0.90	-C.2	8.56	1.13	8.48	1.04	-8.
15409	52.	31.	2.60	1.00	-C.3	11.55	1.20	11.54	1.22	-10.
15410	9.	43.	1.78	1.49	C.3	5.96	1.67	6.12	2.10	2.
15416	29.	68.	1.96	2.00	-1.3	8.56	2.64	8.70	3.01	-30.

Table IV

Summary of Experimental Data

Fifteen runs are listed with information pertinent to calculations. "Counts" is the number of $C^{12}(3+)-\alpha_2$ events observed, $\alpha = (\alpha_1 + \alpha_0)/10,000$ is a measure of the amount of bombardment, and $R_1 = C^{12}(4+)-\alpha_1$ coincidence rate per 10,000 $(\alpha_1 + \alpha_0)$ is a measure of the efficiency. (See text p. 24.)

Run	Target	α slit	Frames		Counts	α	R_1
			First	Last			
1	C6-IX	0.032"	3731	5535	10	332	420±40
2			5588	5893	2	94.8	370±15
3	C6-XII		7581	8897	10	165.0	420±40
4	C7-XVI		9641	10275	7	111.4	460±20
5			10321	11878	18	348.3	530±25
6			12048	12529	6	94.9	510±20
7		0.062	12542	13137	0	34.5	310±15
8		0.060	13146	14897	12	162.3	340±15
9	C6-I		15007	15892	26	422.1	460±20
10		16008	16896	14	225.9	450±30	
11		17008	17895	12	279.0	365±25	
12	C6-VIII		18009	18898	9	424.8	325±20
13		20007	20897	15	421.3	380±15	
14		21012	21896	17	501.5	370±20	
15		22008	22890	12	385.3	305±30	
back-ground	C7-XIV		23008	23284	0	12.2	113±25

Table V

Counting Rates of Observed Charge States

Recoil C^{12} ions from the reaction $C^{12}(He^4, C^{12})He^4$ were observed. The bombarding energies E_1 necessary to give the desired recoil-ion energies are shown, and the counting rate per monitor alpha particle observed with a separate counter in the target chamber is given for each observed charge state. Each entry in the table is an average of three or more runs. The quoted errors are generally the spread of the different readings, except in a few cases in which the statistical error in the number of counts was greater. Entries not observed due to limitations of the equipment are indicated by asterisks (*), and were assumed negligible. (See text p. 29.)

	"Second state"	"First State"	"Ground State"
E_1	3.780 MeV	5.420	7.780
$E(C^{12})$	1.706 MeV	2.511	3.620
0	*	*	*
1+	0.0111±.0002	0.0013±.0001	*
2+	.1009±.0011	.0452±.0002	0.0104±.0002
3+	.1516±.0016	.1774±.0035	.0226±.0003
4+	.0480±.0008	.1201±.0004	.1614±.0034
5+	.0014±.0001	.0082±.0002	.1014±.0007
6+	*	*	.0007±.0000
Σ	0.3129±.0020	0.3522±.0035	0.2965±.0035

CHARGE STATE

Table VI

Ratios of Ionic-Charge States

Charge-state ratios for C^{12} ions are calculated at the three energies measured. The errors shown are just the statistical errors calculated from the data of Table V; the probable systematic error is about double the quoted errors. The average charge \bar{Z} and mean square charge $\overline{Z^2}$ are also listed. (See text pp. 29, 34.)

	"Second state"	"First state"	"Ground state"
$E(C^{12})$	1.706 MeV	2.511	3.620
$v(C^{12})$	5.22×10^8 cm/sec	6.34×10^8	7.62×10^8
0	—	—	—
1+	0.035±0.001	0.0038±0.0001	—
2+	.322±.003	.128±.001	0.035±0.001
3+	.485±.003	.504±.005	.342±.004
4+	.153±.002	.341±.004	.545±.005
5+	.0044±.0003	.023±.001	.076±.001
6+	—	—	.0023±.0003
\bar{Z}	2.769	3.252	3.669
$\overline{Z^2}$	8.243	11.089	13.917

Table VII

Effective Solid Angle for Coincidence Detection

The effects of γ -emission, the elliptical aperture of the spectrometer, and the rectangular alpha slit are included; w and h are the width and height of the rectangular slit in inches, and $d\Omega$ is given in units of 10^{-3} steradian. G is the ratio of $d\Omega$ for the second state to $d\Omega$ for the first state. (See text p. 34.)

w	h	ground	$d\Omega$ first	second	G
0.032"	0.200"	11.1	9.9	8.5	0.866 ± 0.028
.040	.200		10.8	9.7	$.892 \pm .013$
.050	.200		11.1	10.3	$.932 \pm .007$
.060	.200			10.6	$.957 \pm .005$
.062	.245		11.1	10.7	$.959 \pm .005$

Table VIII

Thickness Factors

In the first part of the table, factors necessary to calculate the stopping power ϵ for C^{12} ions in VN at three energies of interest are listed. E_p is the energy of the proton with the same velocity as the C^{12} ion of energy $E(C^{12})$, and ϵ_N and ϵ_V are the nitrogen and vanadium stopping powers for the protons (Reynolds 1953, Bader 1956). $\overline{Z^2}$ is the mean square charge, from Table VI. The second portion of the table then lists the calculated ΔE in keV for various targets. (See text p. 34.) The remaining two sections give the kinematic broadening ΔE_δ and the broadening due to γ -emission, ΔE_γ . (See text p. 35.)

Table VIII
Thickness Factors

	Second state	First state	Ground state
$E(C^{12})$	1.706 MeV	2.511	3.620
E_p	142 keV	209	301
ϵ_N	16.4×10^{-15} eV-cm ²	13.8×10^{-15}	11.1×10^{-15}
ϵ_V	32×10^{-15}	29×10^{-15}	25.3×10^{-15}
$\frac{V}{Z^2}$	8.24	11.09	13.92
ϵ	40×10^{-17} keV-cm ²	48×10^{-17}	51×10^{-17}
TARGET			
C4-XI	120 keV	144	152
C5-I	15	18	19
C6-I	64	78	82
C6-VIII	152	183	193
C6-IX	129	156	164
C6-XII	143	172	181
C7-XVI	55	67	70
$\Delta\delta$	3.0°	2.4	2.4
ΔE_δ	56 keV	55	66
$\Delta\psi$	2.74°	2.14	0
ΔE_γ	163 keV	188	0

Table IX

Momentum Widths of Recoil-Ion Groups

Calculated (calc.) and observed experimental (exp.) values of $\Delta p/p$ for various targets and energies are given. Calculated values are the square root of the sum of the squares of the terms from Table VIII. (See text p. 35.)

Target	Second State	First State		Ground State	
	calc.	calc.	exp.	calc.	exp.
C4-XI	0.062	0.048	0.060	0.023	{ 0.032 .026
C5-I	.051	.039	.041	.010	
C6-I	.054	.042	.039	.017	.020
C6-VIII	.067	.053	{ .049 .050	.028	
C6-IX	.063	.050		.024	
C6-XII	.066	.052		.027	
C7-XVI	.053	.041		.013	

Table X

Thickness Factor T

The fraction of the momentum width of recoil-ion groups from second and first state reactions which lie within the 5% momentum window of the spectrometer are listed. Widths are the calculated $\Delta p/p$ values from Table IX. T is the ratio of the fraction of second state to the fraction of first state within the window. The errors quoted are estimated probable errors. (See text p. 36.)

Target	Second State	First State	T
C6-I	0.93	1.00	0.93±.06
C6-VII	.75	.94	.80±.08
C6-IX	.79	1.00	.79±.08
C6-XII	.76	.96	.79±.08
C7-XVI	.94	1.00	.94±.05

Table XI

Calculation of Weighting Factors W

The weighting factors W are calculated by equation 16 for the data of Table IV, using $P = 3.00 \pm .09$, $C = 1.421 \pm .036$, G from Table VII, and T from Table X. (See text p. 36.)

Run	Target	α	R_1	G	T	$W \times 10^{-4}$
1	C6-IX	332	420	0.866	0.79	4.52±.67
2		94.8	370			1.14±.14
3	C6-XII	165.0	420		.79	2.24±.33
4	C7-XVI	111.4	460		.94	1.98±.17
5		348.3	530			7.12±.62
6		94.9	510			1.87±.16
7		34.5	310	.959		0.46±.04
8		162.3	340	.957		2.35±.16
9	C6-I	422.1	460		.93	8.19±.71
10		225.9	450			4.29±.45
11		279.0	365			4.30±.44
12	C6-VIII	424.8	325		.80	5.01±.62
13		421.3	380			5.81±.67
14		501.5	370			6.74±.81
15		385.3	305			4.26±.45

Table XII

Calculation of $\Gamma_{\text{rad}}/\Gamma$

The weighting factor W (from Table XI) and Counts (from Table IV) are summed for each target, and $\Gamma_{\text{rad}}/\Gamma$ is calculated by equation 16. External error is calculated from the deviations Δ of each value from the mean, and internal error is calculated from the error of $\Sigma(W)$ and $\Sigma(\text{Counts})$. (See text p. 36.)

Target	Counts	$W \times 10^{-4}$	$(\Gamma_{\text{rad}}/\Gamma) \times 10^4$	Δ	$W\Delta^2$
C6-IX	12	$5.66 \pm .68$	$2.12 \pm .66$	-0.70	2.77
C6-XII	10	$2.24 \pm .33$	4.46 ± 1.56	+1.64	6.02
C7-XVI	43	$13.78 \pm .68$	$3.12 \pm .50$	+0.30	1.24
C6-I	52	$16.78 \pm .95$	$3.10 \pm .47$	+0.28	1.31
C6-VIII	53	21.82 ± 1.30	$2.43 \pm .37$	-0.39	3.32
Σ	170	60.28 ± 1.91	$2.82 \pm .23$ (internal) $2.82 \pm .22$ (external)		

-71A-

Figure 1

Energy Level Diagram of C^{12}

The level of interest is the 7.656-MeV level. The drawing is from Lauritsen and Ajzenberg-Selove (1962); for explanation of conventions followed see Ajzenberg-Selove and Lauritsen (1959). (See text pp. 2, 4, 5, 32.)

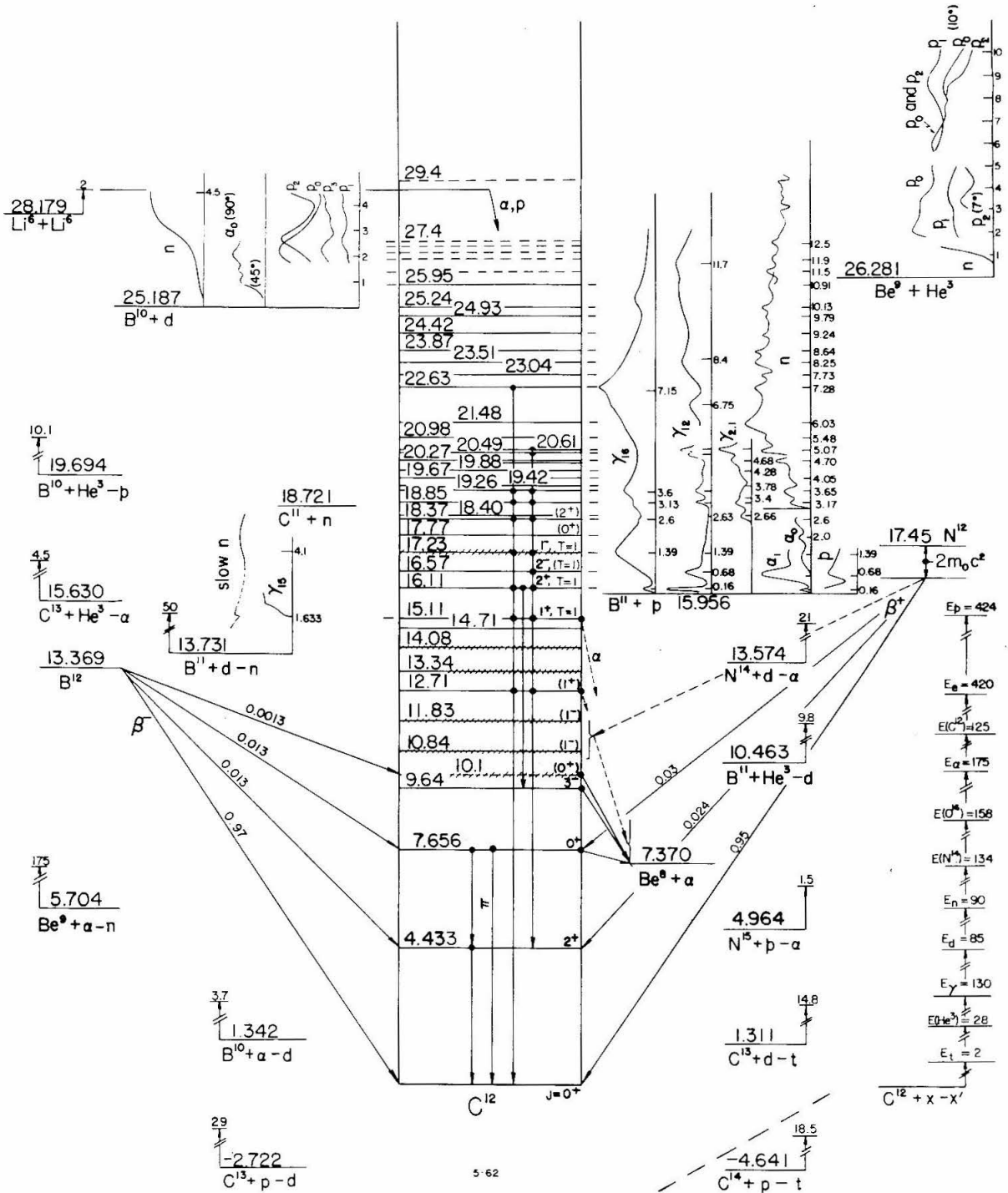


FIGURE I.

Figure 2

Plan of Experiment

The arrangement of the equipment used in the experiment is shown. Recoil C^{12} ions at 90° were analyzed and detected, and the pulses amplified; alpha pulses from a counter in the target chamber were delayed so as to coincide with the C^{12} pulses; and whenever a coincidence occurred the two pulses were displayed on the dual-beam oscilloscope and photographed. (See text pp. 5-15; recoil-ion detection p. 7, alpha detection p. 9, coincidence detection p. 12.)

-73A-

Figure 3

Nitriding Chamber

Targets were nitrated by heating in an ammonia atmosphere. The heating was accomplished by bombardment with an alpha-particle beam at the straight-through port of the accelerator. Ammonia was admitted from the stainless-steel flask cooled to dry ice temperature; flow was controlled by a needle valve. The efficiency of the differential pumping and cold trap arrangement shown was such that an ammonia pressure of 1 mm Hg read on the thermocouple gauge caused no increase in the pressure reading of the accelerator column. Note that the beam passes through a length of copper tubing soldered to a copper rod leading to the cold trap. (See text p. 7, Appendix A.)

NITRIDING CHAMBER

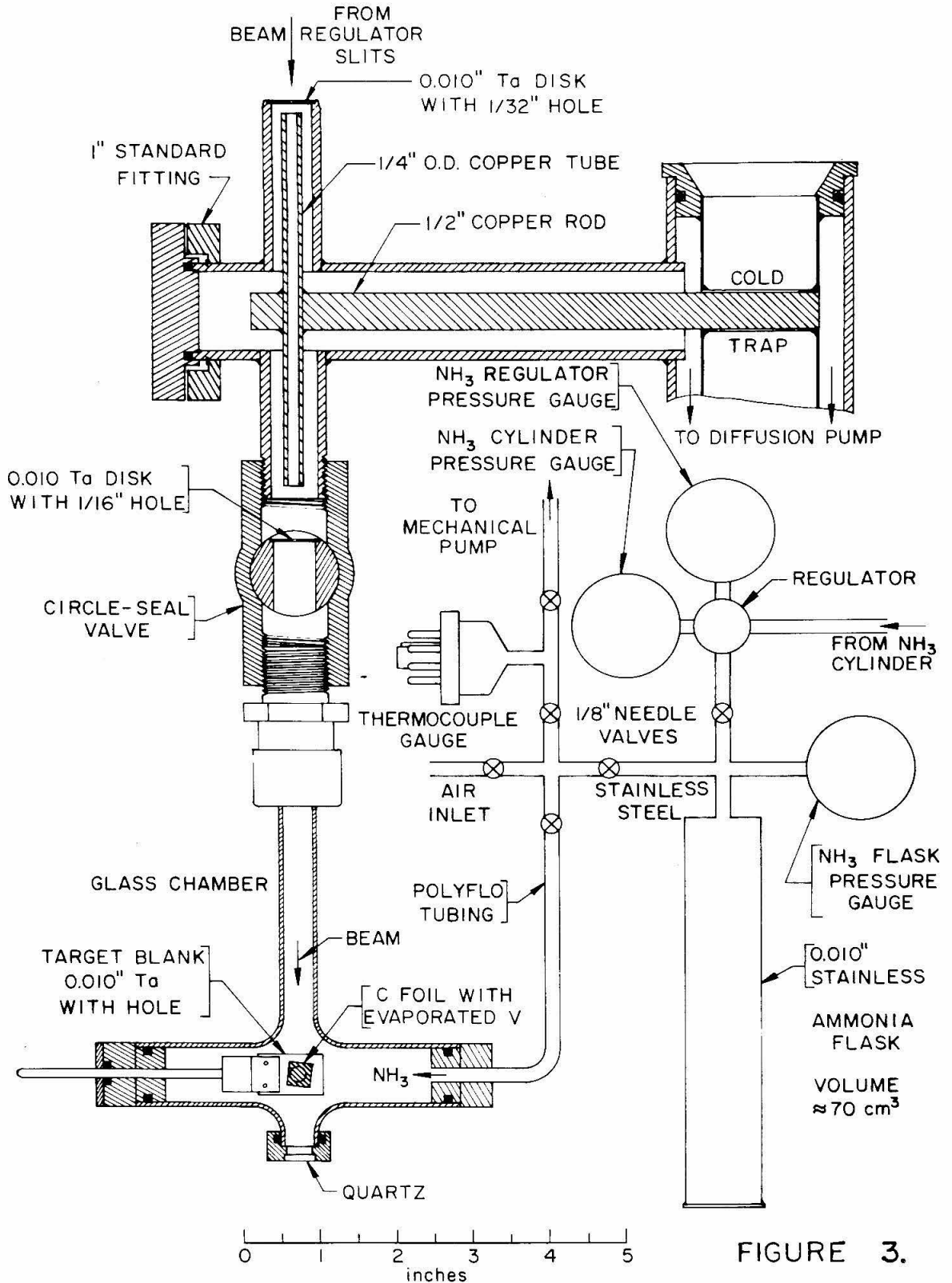


FIGURE 3.

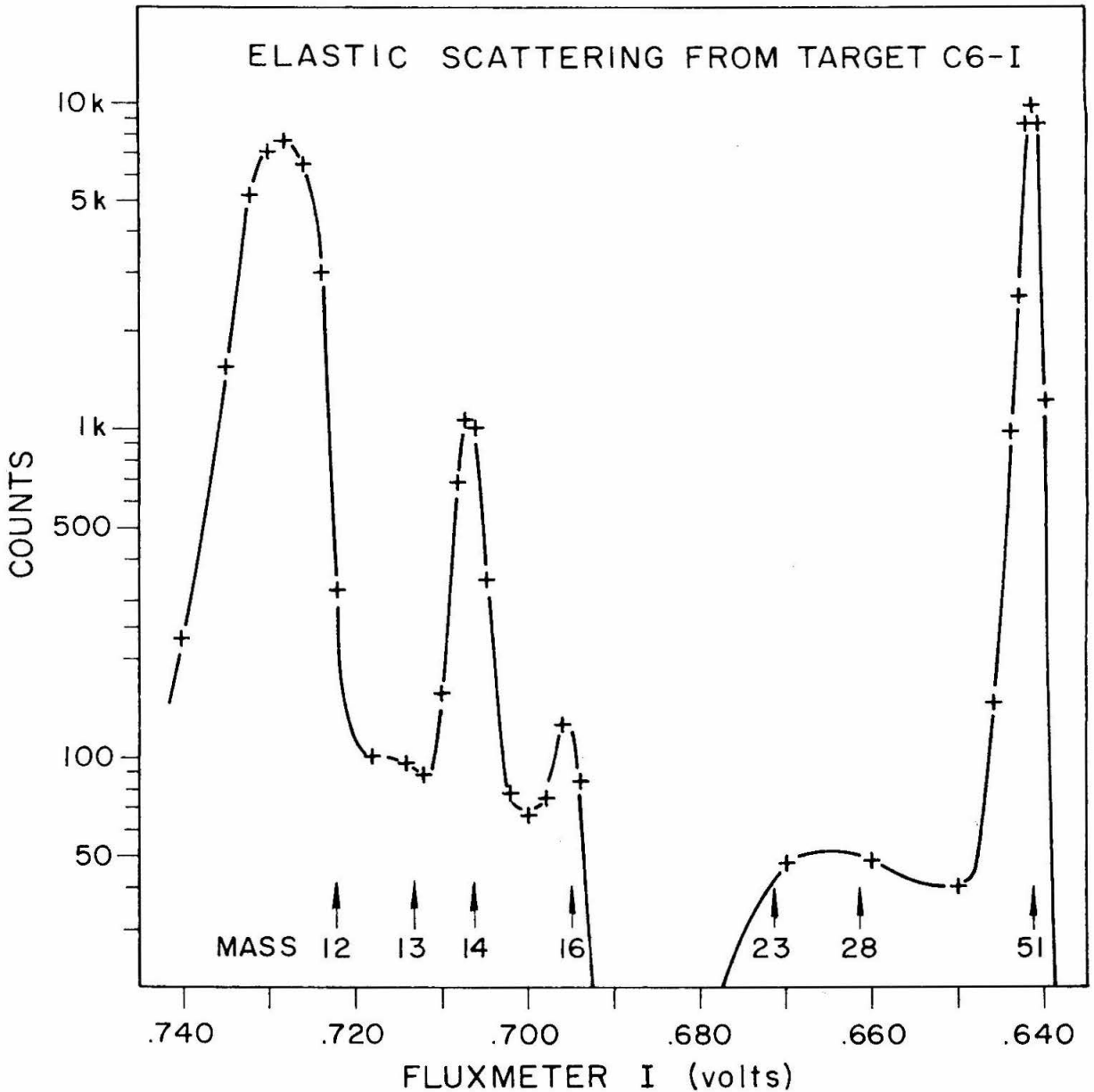


FIGURE 4.

Elastic Scattering from Target C6-I

The momentum spectrum of elastically scattered protons of 1-MeV incident energy, as measured with a 10½-inch magnetic spectrometer at a laboratory angle of 150°, is shown. The arrows indicate the locations of groups scattered from various masses, normalized to the V⁵¹ peak. (See text p. 7, Appendix A.)

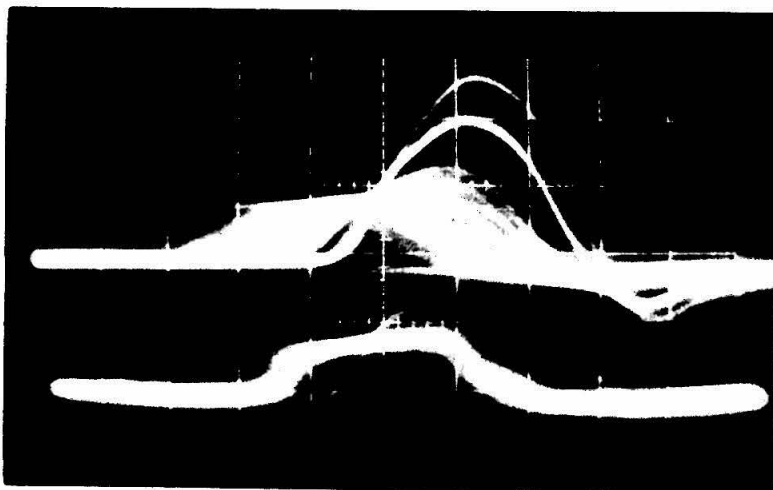


FIGURE 5a.

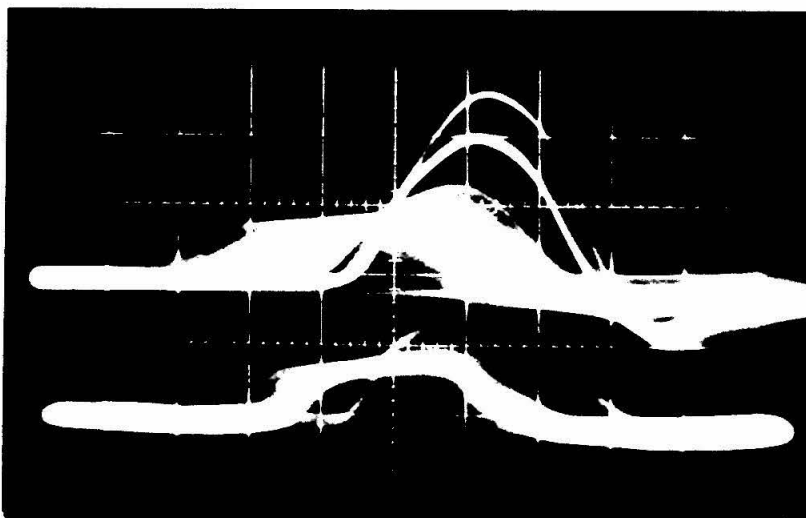


FIGURE 5b.

Non-Coincident Spectra

These two prints (from the same negative) show the non-coincident alpha spectrum on the upper beam and the spectrum at the magnet focus on the lower beam of the dual-beam oscilloscope. (See text pp. 9, 11, 19.) Figure 5a shows barrel distortion as it occurs on the negative; in Figure 5b the distortion has been removed by using the camera lens as an enlarger. (See text p. 15, Appendix B.)

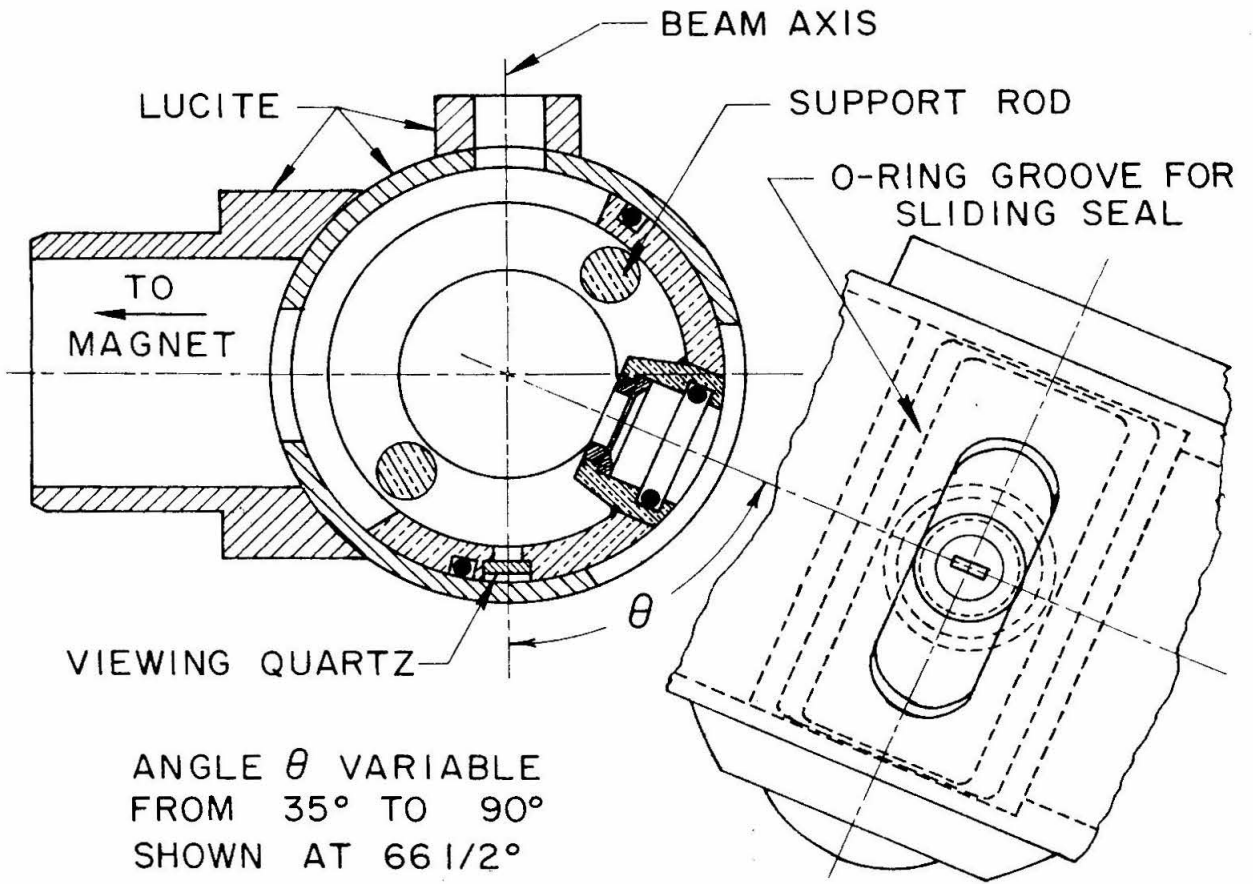
-76A-

Figure 6

Variable Angle Target Chamber

The counter angle θ in this chamber is continuously variable from 35° to 90° . The "rectangular" slit, mounted in the counter holder $5/8$ inch from the center of the chamber, determines the solid angle of the detector; slits of various sizes were made. For details of the chamber, see Kellogg drawing #1B2-75. (See text p. 9.)

VARIABLE ANGLE TARGET CHAMBER



FULL SIZE
SEE DRAWING # 1B2 - 75

"RECTANGULAR" SLIT DETAIL
2 1/2 TIMES SIZE

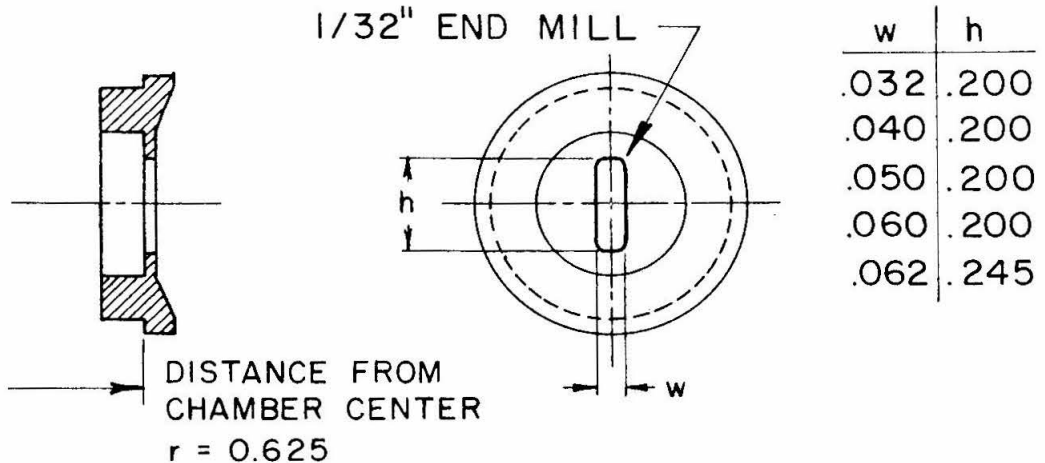


FIGURE 6.

COUNTER MOUNT FOR VARIABLE θ CHAMBER

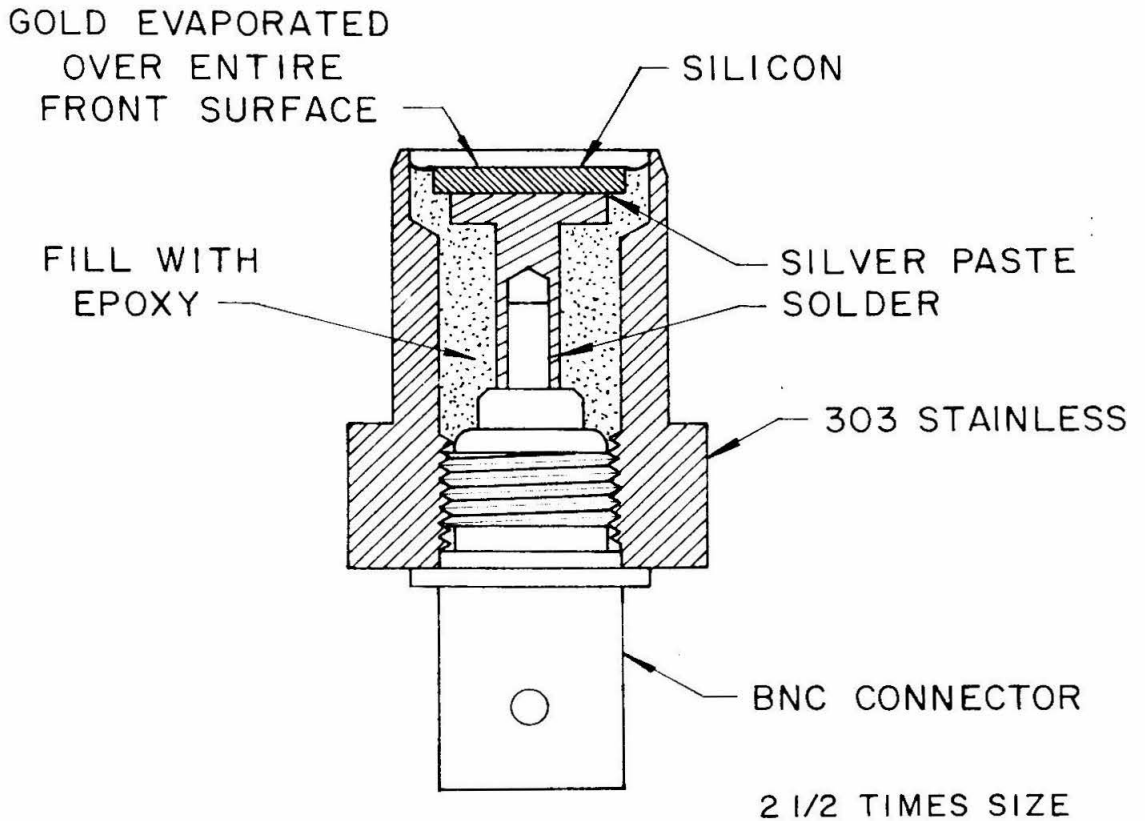
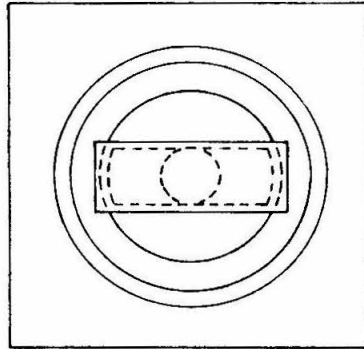


FIGURE 7.

Counter Mount for Variable Angle Chamber.

The gold evaporated onto the silicon to make a rectifying junction also makes contact with the grounded case. The signal lead makes ohmic contact to the rear surface of the silicon. (See text p. 10.)

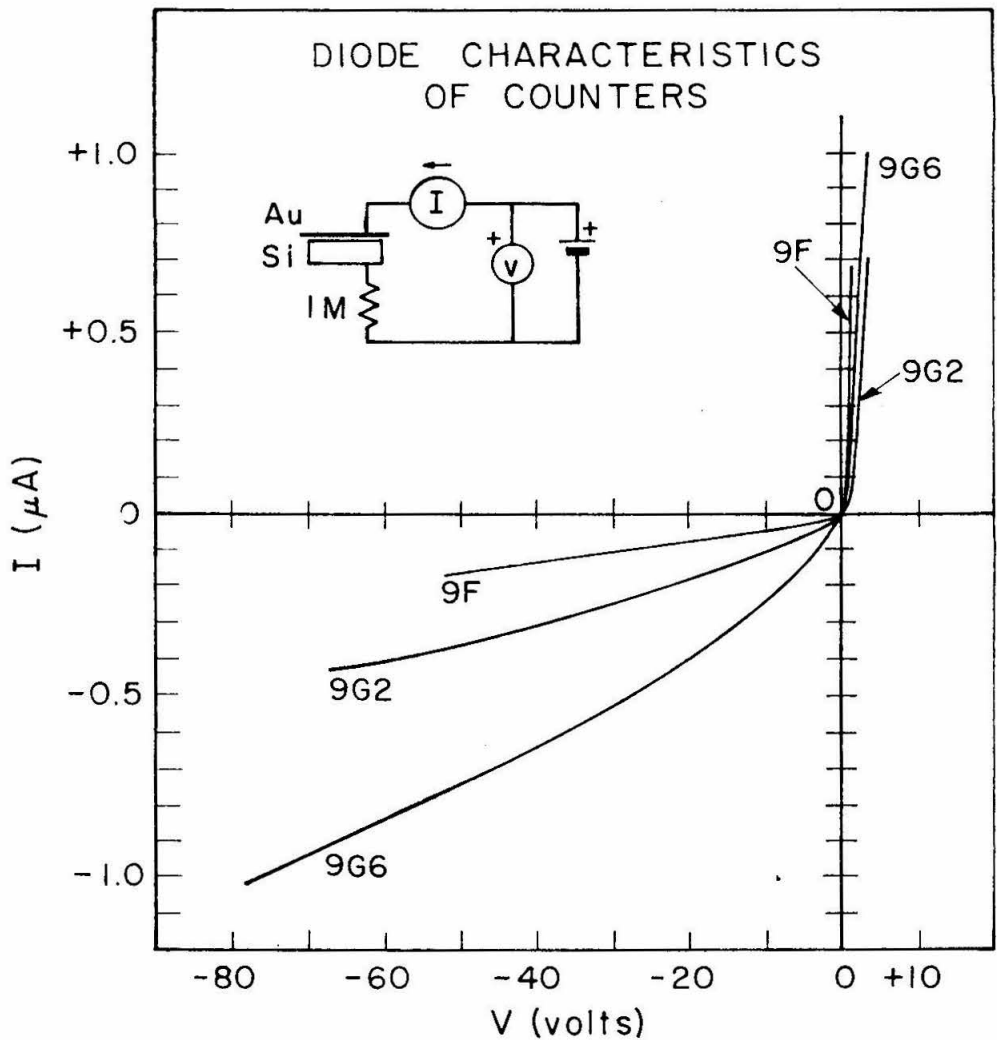


FIGURE 8.

Diode Characteristics of Counters

The forward and reverse current-voltage characteristic of gold-silicon surface-barrier counters was measured as indicated in the figure. The three units displayed here, made with 900 Ω -cm silicon, were all successful counters. In use, a reverse bias of about 50 volts was applied. (See text p. 10.)

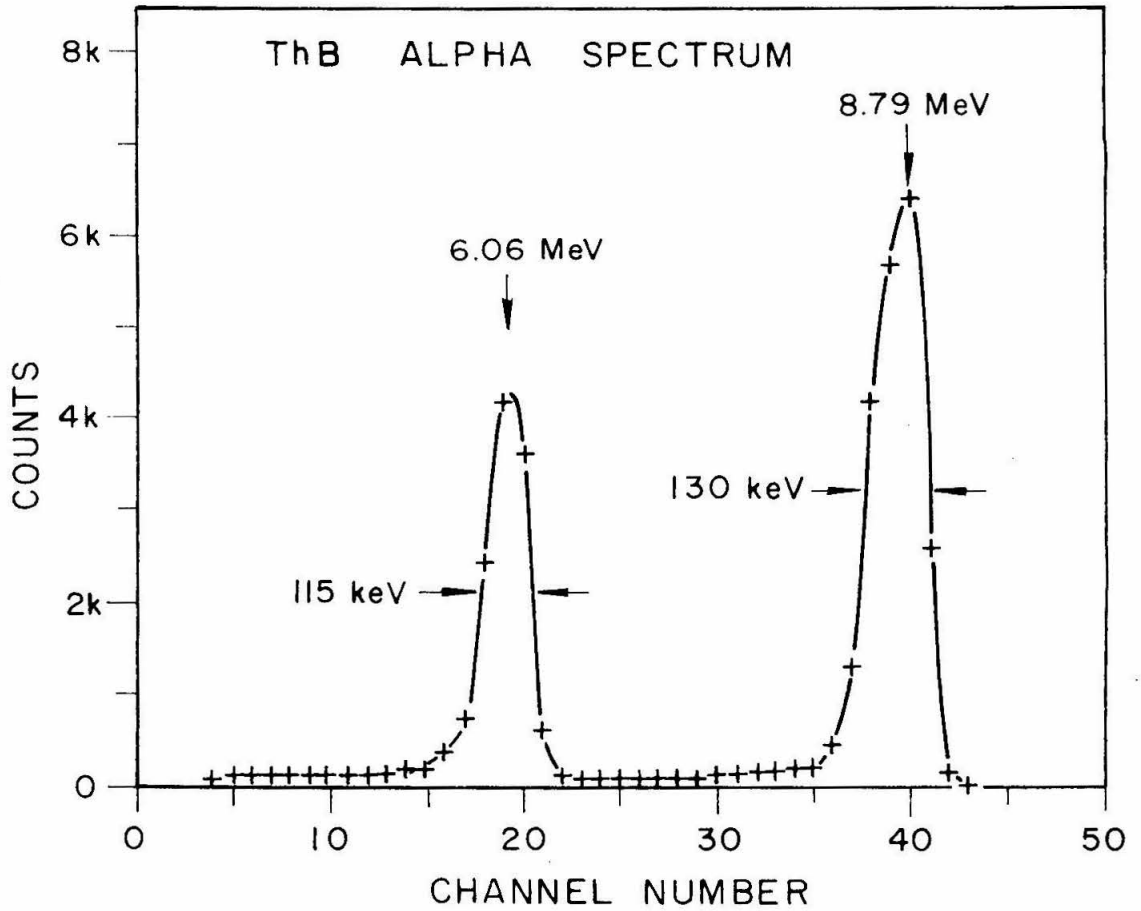


FIGURE 9.

ThB Alpha Spectrum

This spectrum was taken with counter 9F and the alpha-channel electronics of Figure 2. The amplifier bias corresponds to 3.52 MeV. (See text pp. 10, 17.)

Figure 10

Coincidence Mixer

Tunnel diodes are used at both inputs of the mixer as discriminators, and a tunnel diode is also used for the mixer. The output for a pulse at either input sufficient to trigger the diode is a 20-V, 2- μ sec pulse. Note that the coincidence-pulse output was from point B, with a 220-ohm plate load on the output tube. This pulse was used to trigger the oscilloscope sweep. (See text p. 12.)

Figure 11

35-mm Oscilloscope Camera

The camera is designed to use a Nikkor $f/1.1$ lens and a Beattie-Coleman electric film magazine. The magnification is $1/3$. The locations of the focal planes F and F' and the corresponding principal planes H and H' are shown measured in inches from the rear surface of the mounting ring when the distance setting on the lens is 6 feet. (See text p. 14, Appendix B.)

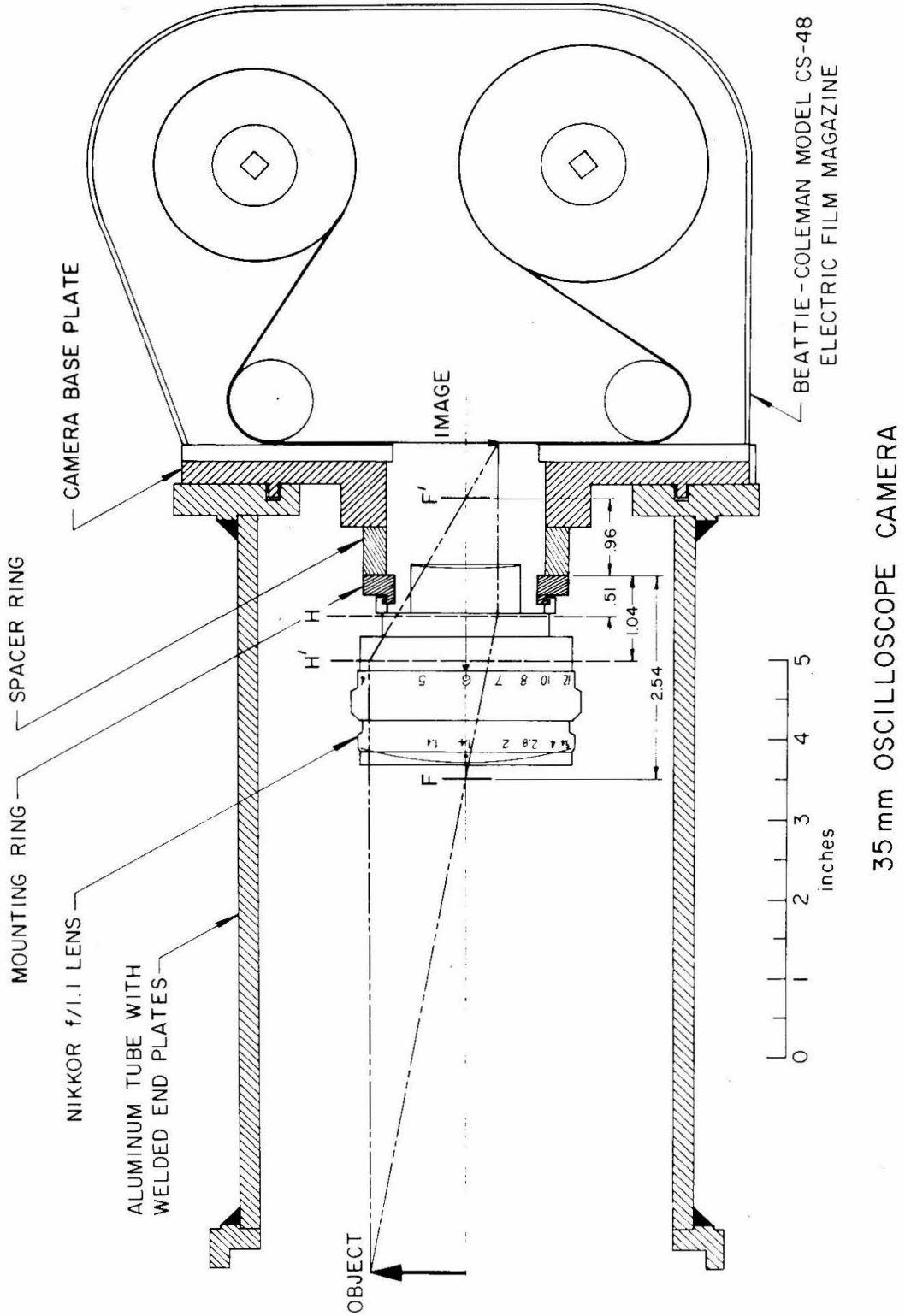


FIGURE 11.

Figure 12

Film-Advance Circuit

A suitable pulse (e.g. 8-V, 0.6- μ sec) at the "trigger in" switches the silicon controlled rectifier (SCR) to its conducting mode, and current through the 10K resistor holds it conducting while the current in the relay coil builds up. When the relay closes, current is supplied to the film-advance motor. When the film has moved far enough to open the cam-operated microswitch, the relay opens and the SCR is turned off; current is then supplied to the motor through the microswitch until the film has advanced one frame. The relay is also used to operate a Sodeco counter which is used to count frames on the film. (See text p. 15, Appendix B.)

FILM-ADVANCE CIRCUIT

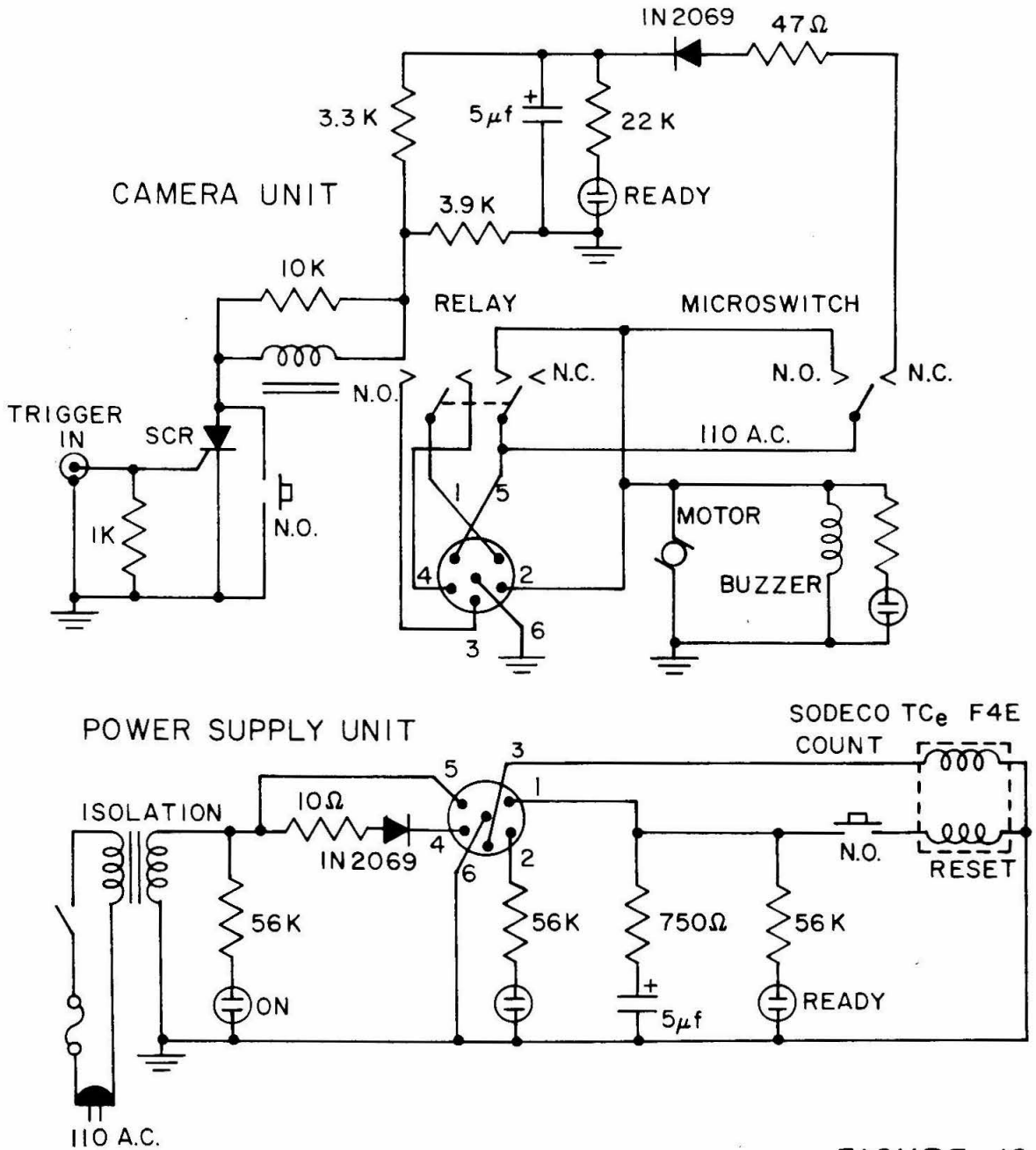
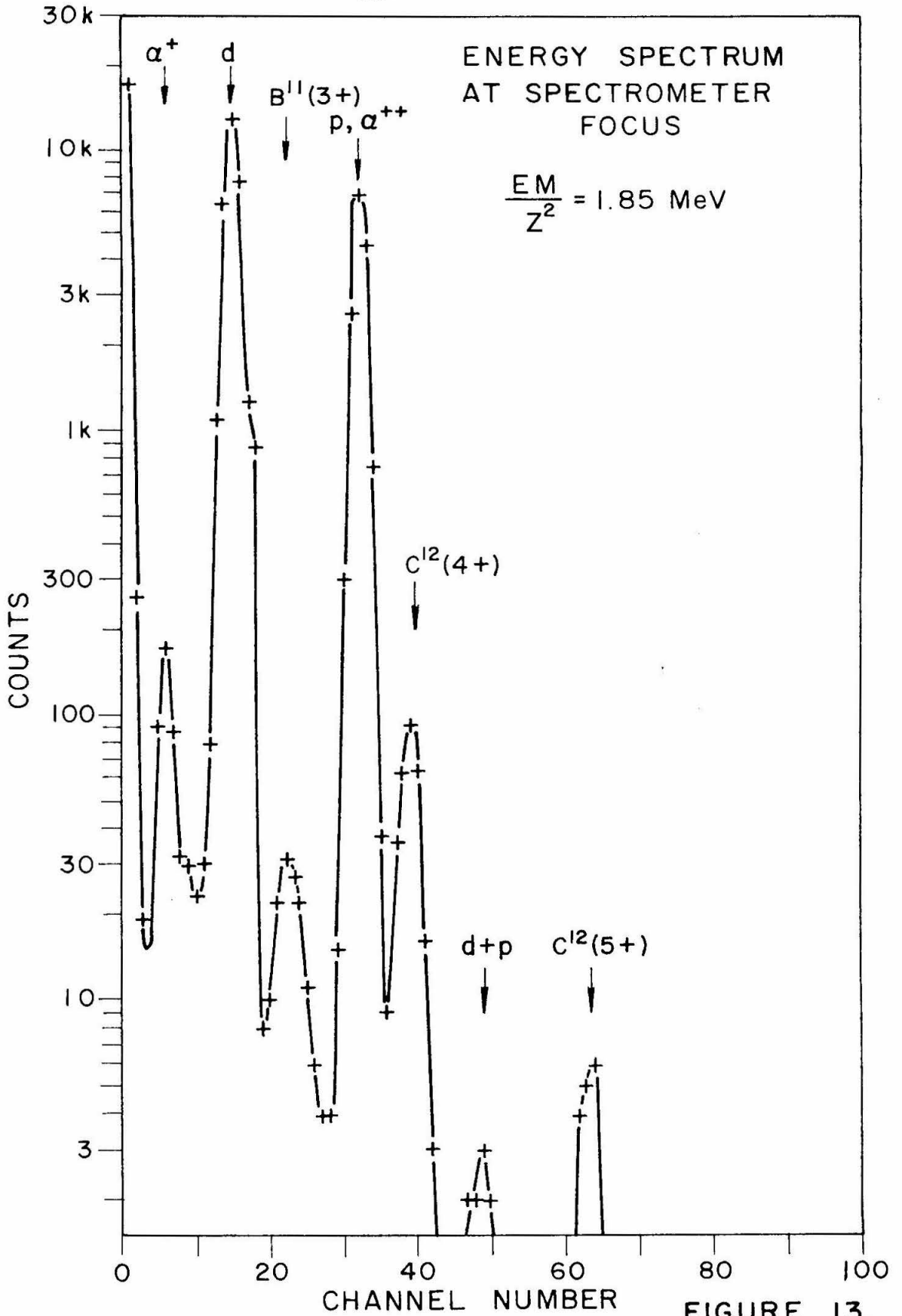


FIGURE 12.

Figure 13

Energy Spectrum at Spectrometer Focus

In addition to elastically scattered deuterons and reaction products (p and α), three recoil-nucleus groups appear in this spectrum, taken with a solid-state counter at the focus of the alternating-gradient spectrometer. The spectrometer momentum resolution was 1.3%, the flux-meter setting was $1/I^2 = 16.5$, and the spectrum is normalized to 20,000 alphas observed in the chamber counter. (See text p. 16.)



Energy-Momentum Survey

The counting rate as a function of magnetic-spectrometer-fluxmeter setting and multichannel-analyzer address is represented by the contour lines. Each contour represents a factor of ten in the counting rate. Ground-state C^{12} nuclei were observed with charges between (3+) and (6+), and first-state C^{12} recoils were observed with charges between (2+) and (5+). Diagonal lines with slopes Z^2/M are drawn to identify the various types of particles. The effect of the dead layer of the gold-silicon surface-barrier counter used is to cause the loci of the heavy-ion groups to intersect zero momentum at -11 channels on the energy scale. Contours for the broad proton groups of energy greater than 3 MeV, which penetrated the depletion layer, are not shown. The heavy cross indicates the location of the second-state $C^{12}(3^+)$ recoil-ion group; note that it is in a region of low background. A typical spectrum from which this plot was derived is shown in Figure 13. (See text pp. 16, 35.)

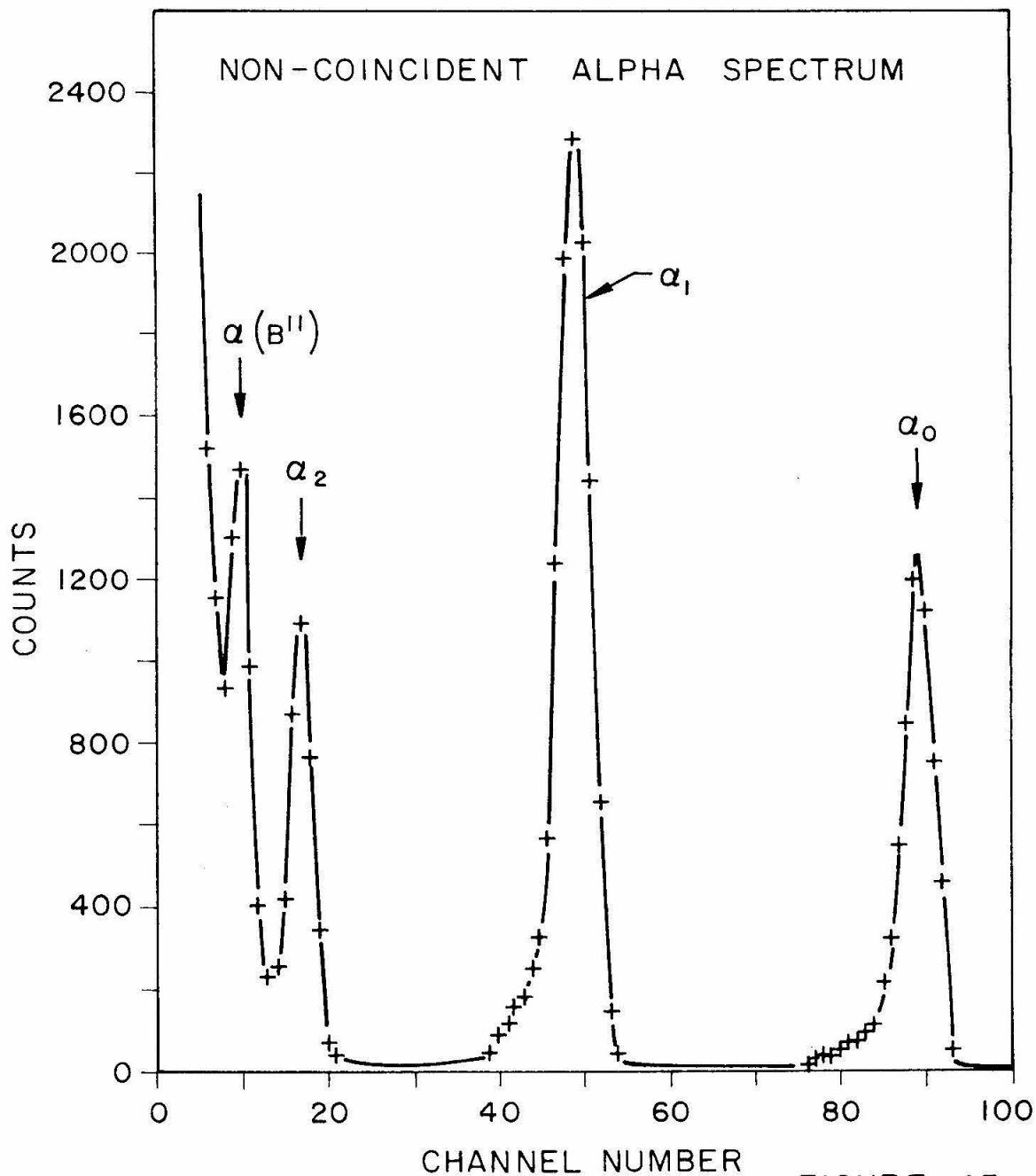


FIGURE 15.

Non-Coincident Alpha Spectrum

This alpha spectrum from the reaction $N^{14}(d, \alpha)C^{12}$ was taken with the electronics of Figure 2. The counter angle was 67° (lab), and the deuteron bombarding energy was 1.800 MeV. The bias level of the biased amplifier was about 4 MeV. (See text pp. 17, 18, 28.)

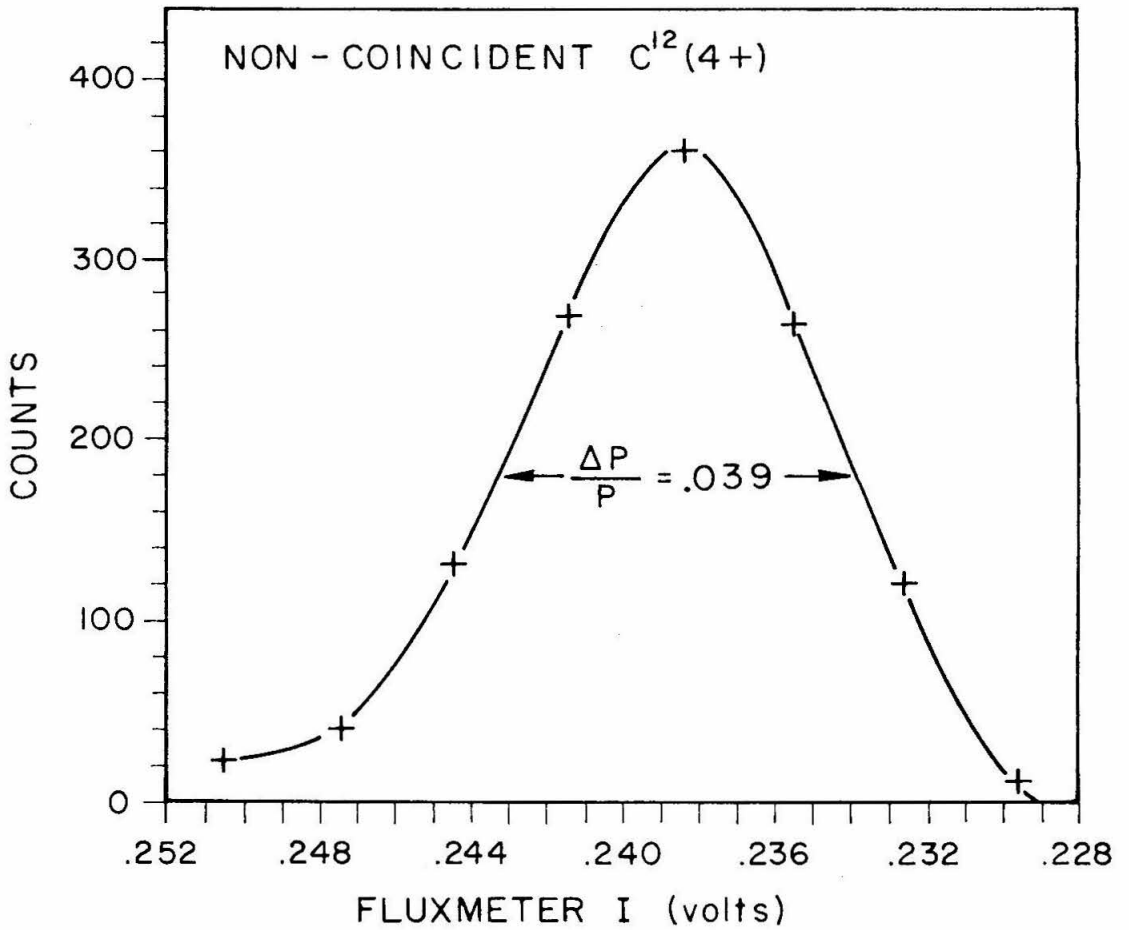


FIGURE 16.

Non-Coincident $C^{12}(4+)$

The spectrometer current was varied to find the maximum $C^{12}(4+)$ counting rate. The 1.3% momentum resolution slit was used. This is also a measurement of the momentum width of the recoil-ion group; target C6-I was used for these data. (See text pp. 17, 35.)

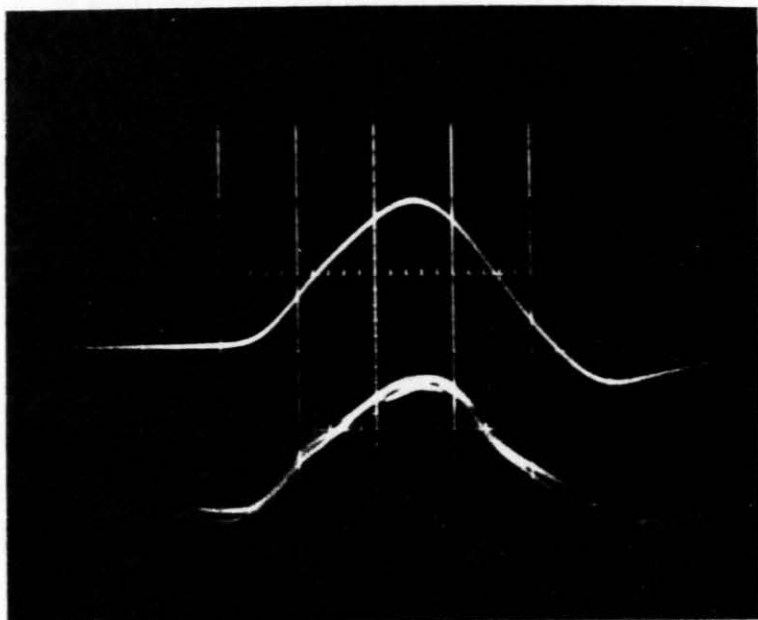


FIGURE 17.

$C^{12}(4^+)-\alpha_1$ Coincidences

This is a multiple exposure showing five triggered sweeps of the dual-beam oscilloscope, with the spectrometer current, alpha angle, and delay set to the values appropriate to $C^{12}(4^+)-\alpha_1$ coincidences. The alpha-particle pulses are on the upper beam, and the recoil-ion pulses on the lower beam. The vertical scale for each beam is 0.5 V/cm, and the common time base is 20 nsec/cm. Note that the higher gain necessary for the lower energy C^{12} pulses results in a higher relative noise level. (See text pp. 17, 21.)

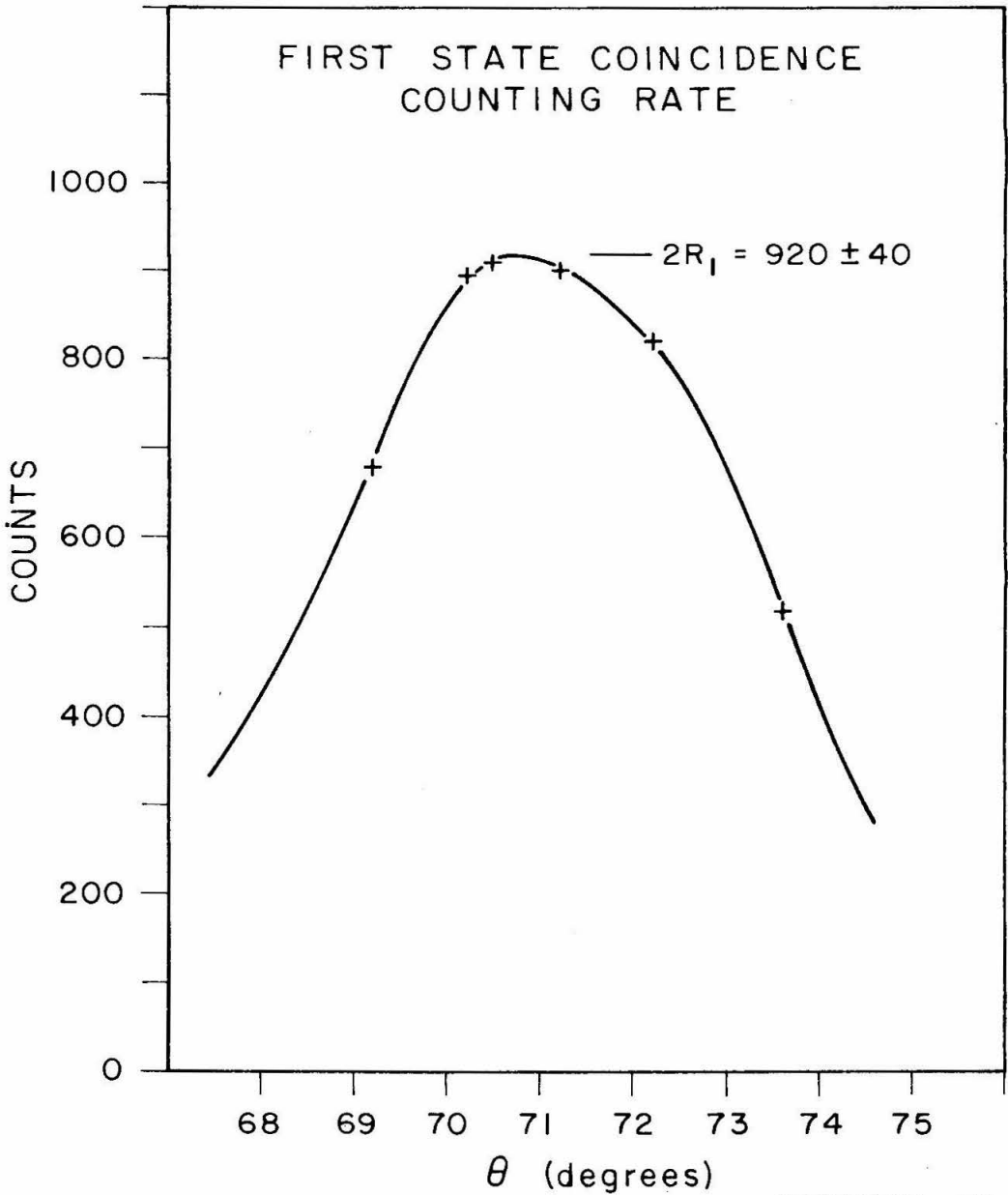


FIGURE 18.

First-State Coincidence Counting Rate

With the spectrometer current and delay set, the alpha counter angle θ was varied to find the maximum $C^{12}(4^+)-\alpha_1$ coincidence counting rate. The curve is normalized to 20,000 $(\alpha_1 + \alpha_0)$ alpha particles, and hence the maximum rate is $2 R_1$. (See text p. 17.)

Figure 19

Portion of $30 \times 27 \times 20$ Array for Film #15

The three central sections of the computer output are shown.

Figure 19a is the 30×27 array of counts vs. alpha energy and recoil-ion energy for $\Delta t = -5$ nsec (time of flight = 157 nsec). Figures 19b and 19c are the arrays for $\Delta t = 0$ ($t = 162$) nsec and $\Delta t = 5$ ($t = 167$) nsec. The circled group, containing 26 counts, is $C^{12}(3+)$ in coincidence with α_2 . (See text p. 22.) Figure 19d is the center section of the array made up of the sum of all data, and corresponds to Figure 19b for film #15.

Correlated Coincidence Spectrum

The number of counts (area scale at right) is plotted as a function of the energies of the coincident particles, E_{C12} and $E_{Q'}$, and the difference Δt of the time of flight from 162 nsec. The figure is most easily interpreted by using color to identify the vertical (Δt) scale. (See footnote on p. 22.) The height of each point above the base plane can be found by comparing its color to the scale at the left. Then the two energies can be found by projecting the point onto the base plane. The group of interest is the red ($\Delta t = 0$) group at $E_{C12} = 1.7$ MeV and $E_{Q'} = 6.1$ MeV. The remaining features are discussed in the text. (Pp. 22-23.)

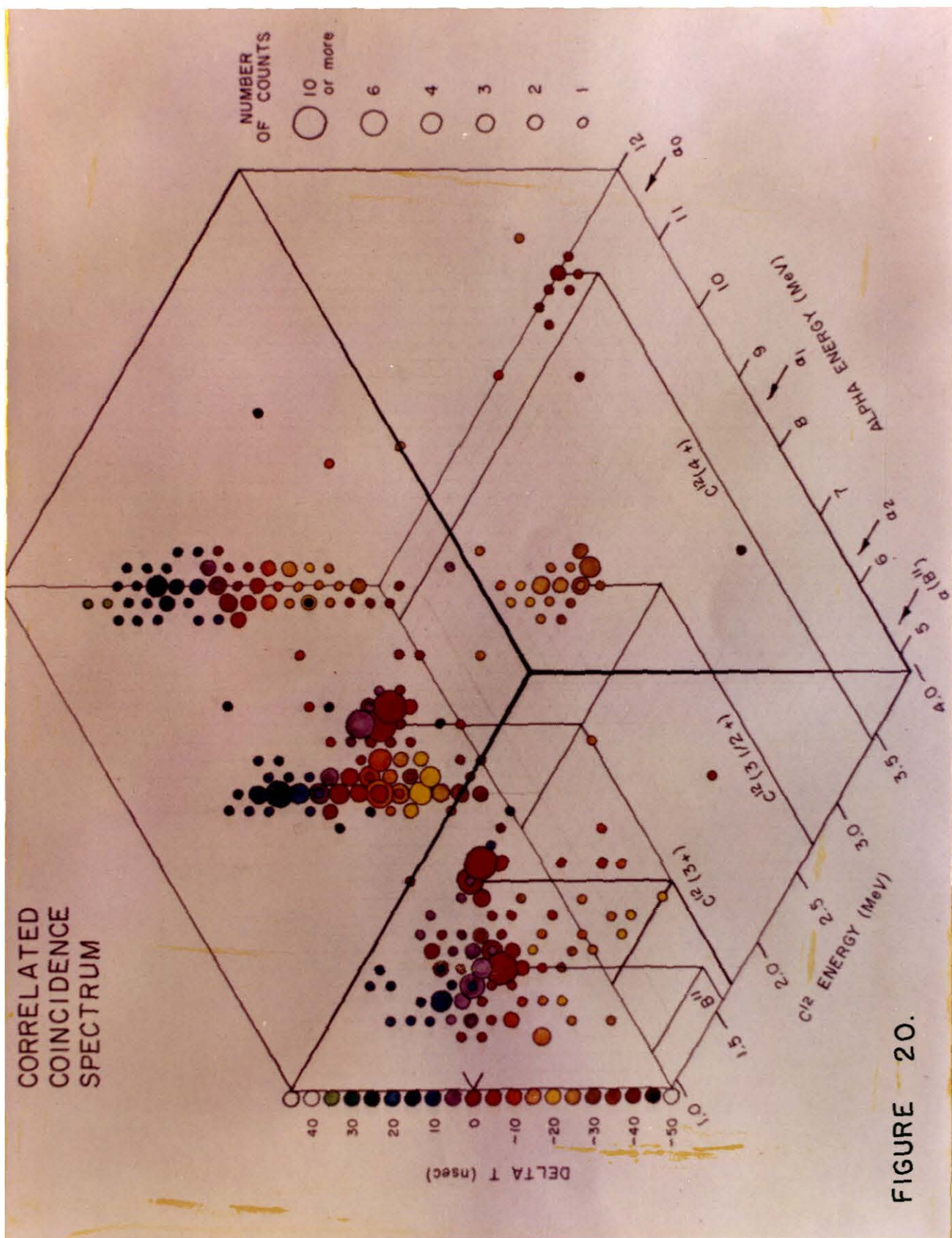


FIGURE - 20.

Figure 21

Uncorrelated Coincidence Spectra

The three histograms are the projections of the data in Figure 20 onto the three axes. The solid areas are the events of interest, $C^{12}(3^+)-\alpha_2$ coincidences. Note that they cannot be distinguished on the basis of these uncorrelated spectra; they were identified from Figures 19 and 20. (See text pp. 13, 24.)

UNCORRELATED COINCIDENCE SPECTRA WITH RESPECT TO
 DELTA T, α ENERGY, AND C^{12} ENERGY

▨ Deuterons in C^{12} Channel

■ $C^{12}(3+)-\alpha_2$ Events

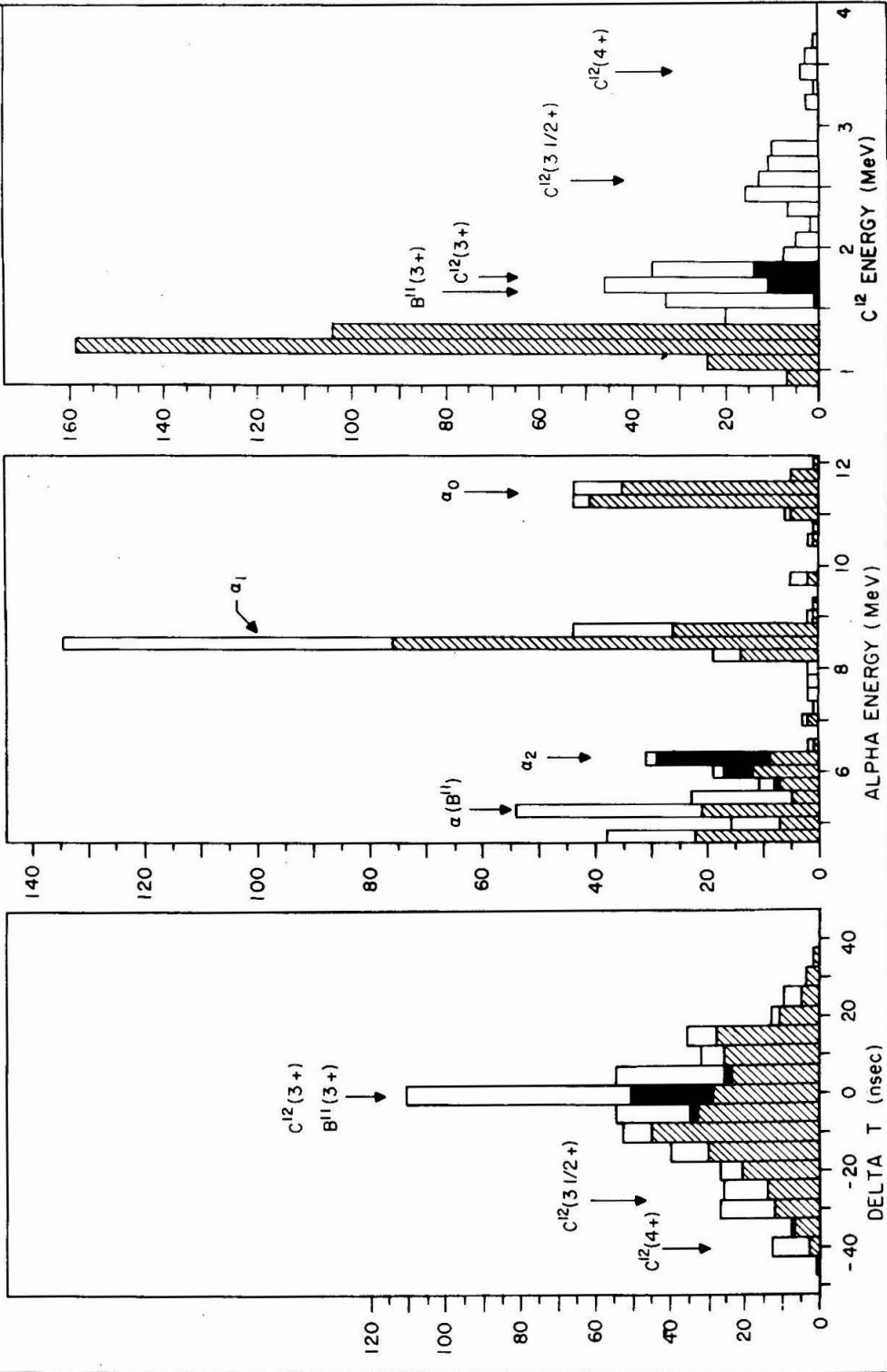
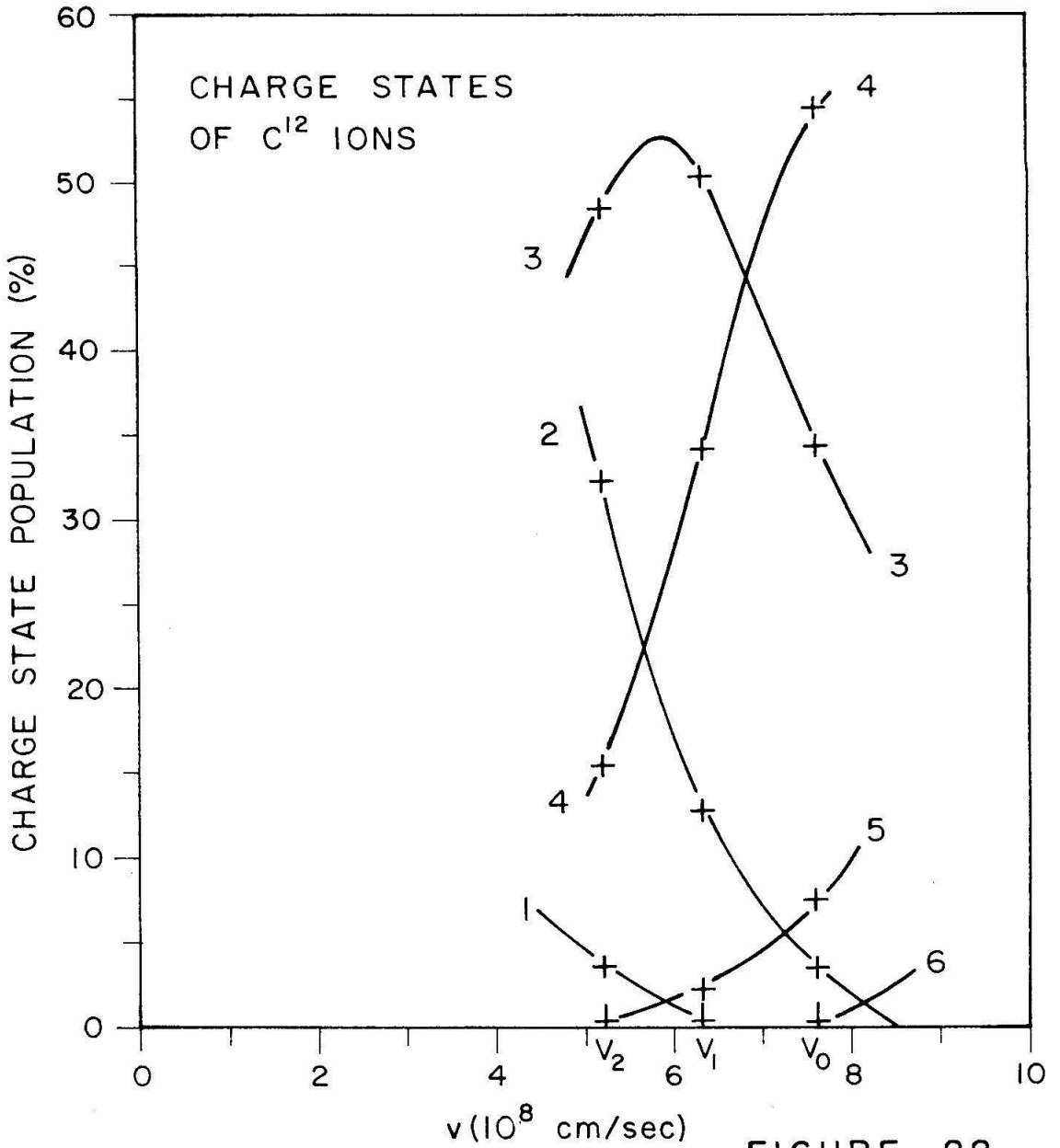


FIGURE 21 a

b

c



Charge States of C¹² Ions

FIGURE 22.

The charge ratios listed in Table VI are plotted vs. the velocity of carbon ions. The three velocities v_0 , v_1 , and v_2 correspond to recoil-C¹² ions from N¹⁴(d, α)C¹² reactions involving ground-state, first-state, and second-state events, respectively. (See text p. 30.)

NOTATION FOR SOLID ANGLE CALCULATIONS

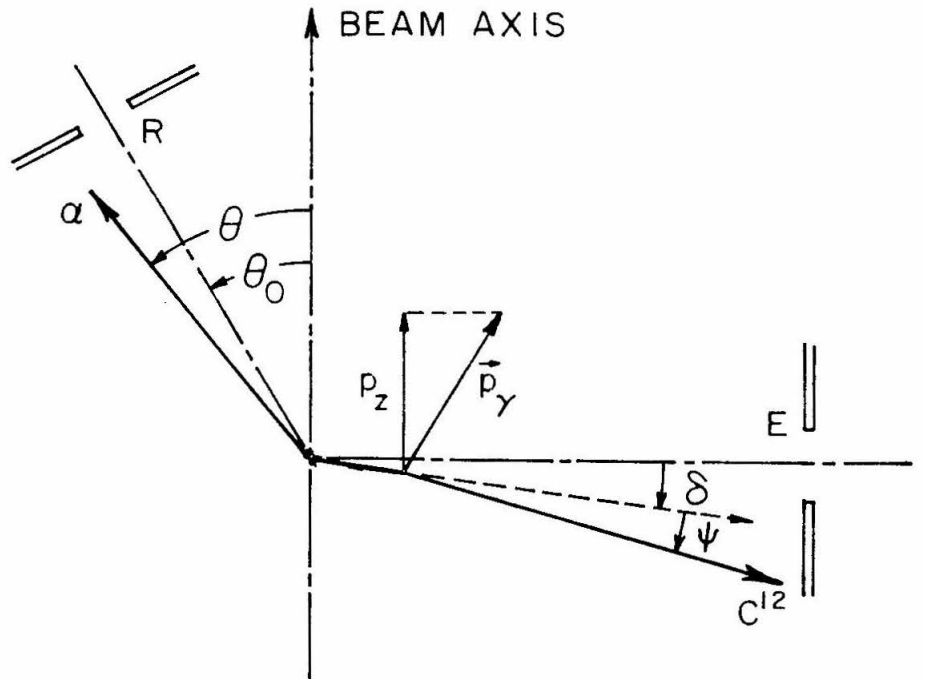


FIGURE 23.

Notation for Solid Angle Calculations

The angle θ_0 is the center of the rectangular slit R, and is the alpha angle corresponding to a recoil-ion angle of 90° . Angles $90^\circ + \delta$ and θ are the C^{12*} and α directions after the $N^{14}(d, \alpha)C^{12*}$ reaction. The recoil ion is deflected by gamma emission; the horizontal projection of the deflection is the angle ψ . The component of the gamma momentum vector \vec{p}_γ parallel to the beam axis is p_z . (See text p. 31, Appendix C.)

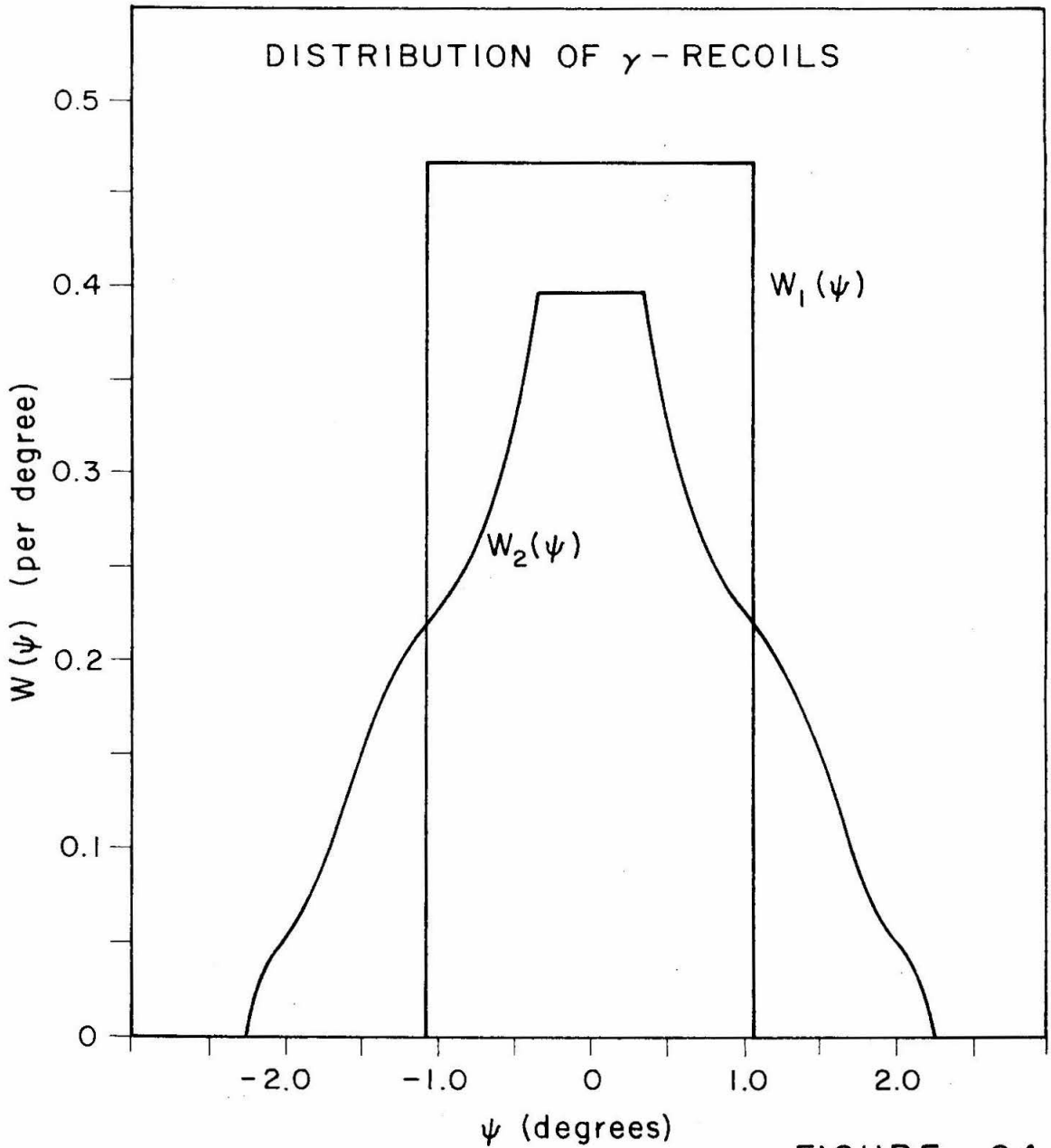


FIGURE 24.

Distribution of γ -Recoils

$W(\psi)d\psi$ is the probability that the projection in the horizontal plane of the deflection of a recoiling C^{12*} nucleus by gamma emission will be between ψ and $\psi + d\psi$. W_1 refers to C^{12} nuclei formed in the first excited state, and W_2 refers to second-state nuclei. These curves also represent the probability distributions for a single component of the gamma momentum. (See text p. 32, Appendix C.)

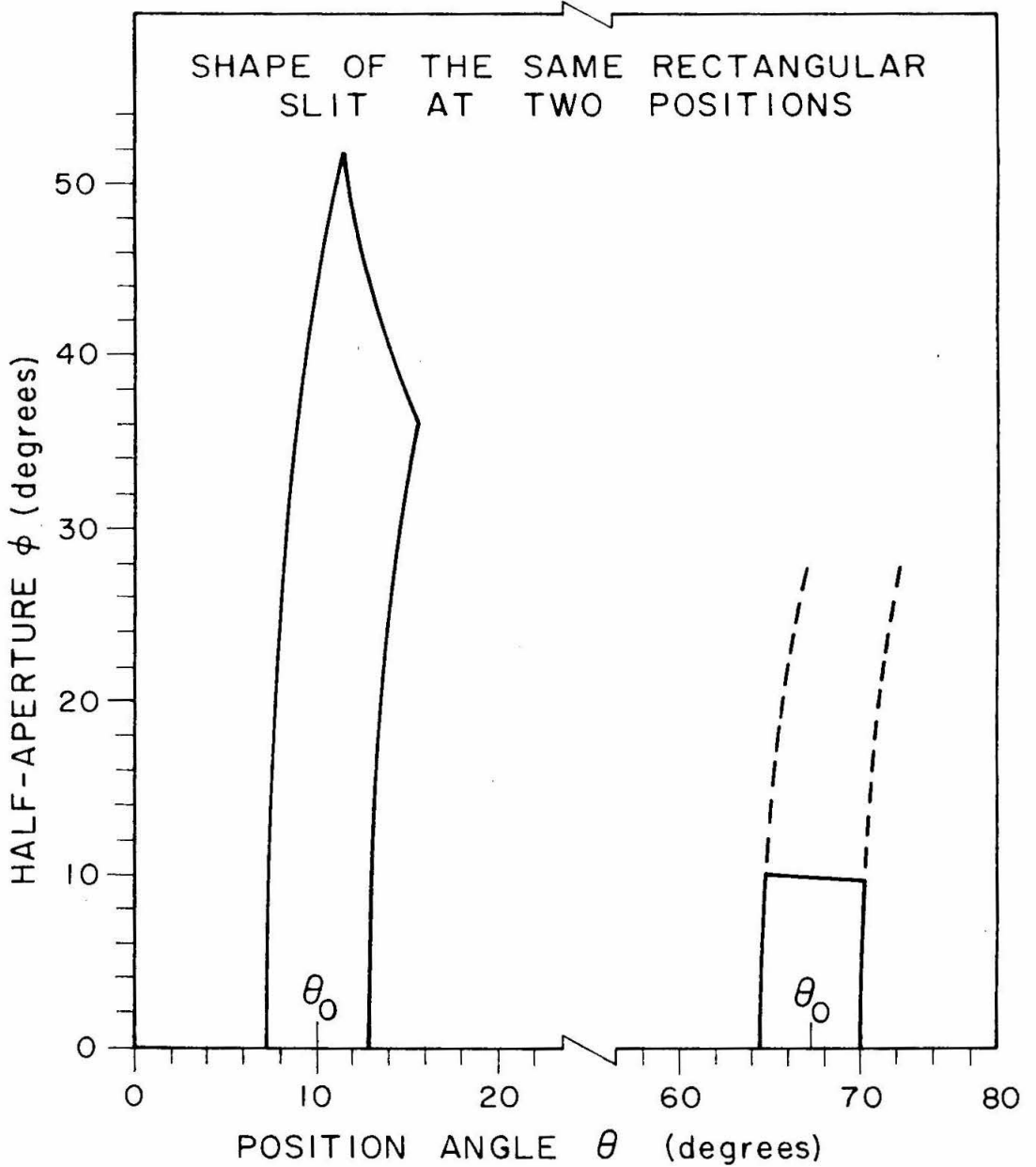


FIGURE 25.

Shape of Rectangular Slit

The shape of the 0.060-inch wide, 0.200-inch tall alpha slit is shown as projected on a sphere at two different positions. (See text p. 33, Appendix D.)

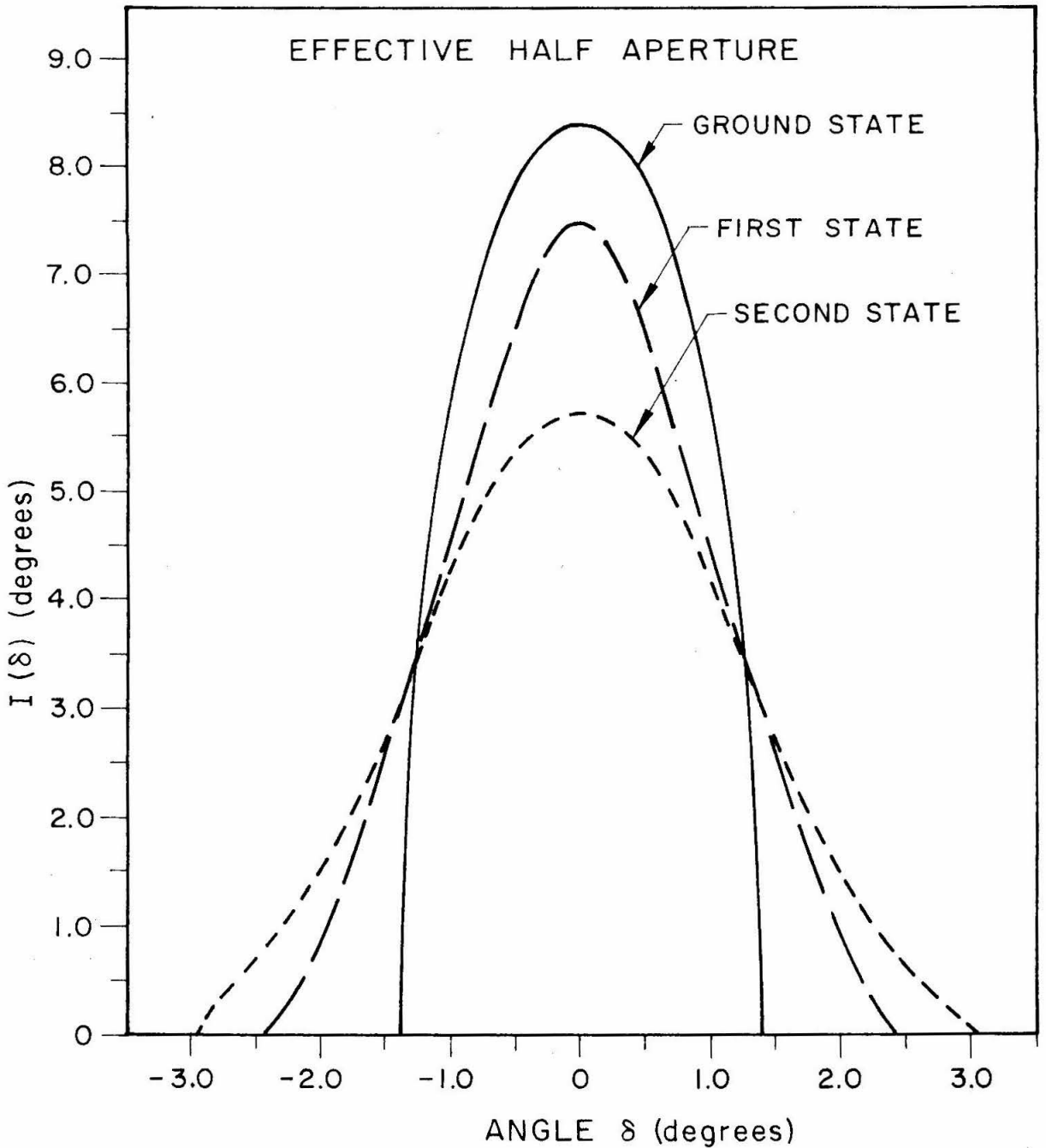


FIGURE 26.

Effective Half Aperture

The function $I(\delta)$ is effectively the probability that a C^{12} ion initially deviating from 90° by an angle δ will be detected in coincidence with its alpha particle. For the ground state this is just the shape of the spectrometer aperture. (See text pp. 33, 35.)

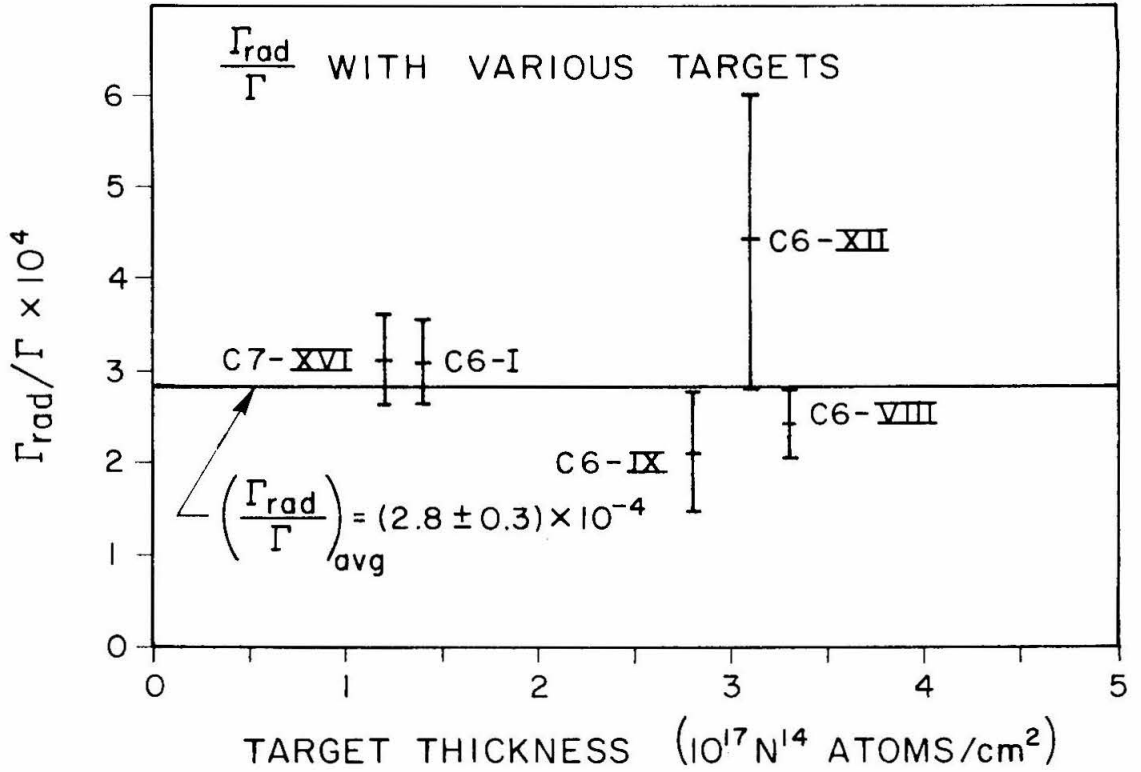


FIGURE 27.

$\Gamma_{\text{rad}}/\Gamma$ with Various Targets

The sum of the results from each of the five targets used to obtain data are displayed vs. target thickness, to show that target thickness effects have been fairly well accounted for. The average of all data is $\Gamma_{\text{rad}}/\Gamma = (2.8 \pm 0.3) \times 10^{-4}$. (See text p. 36.)

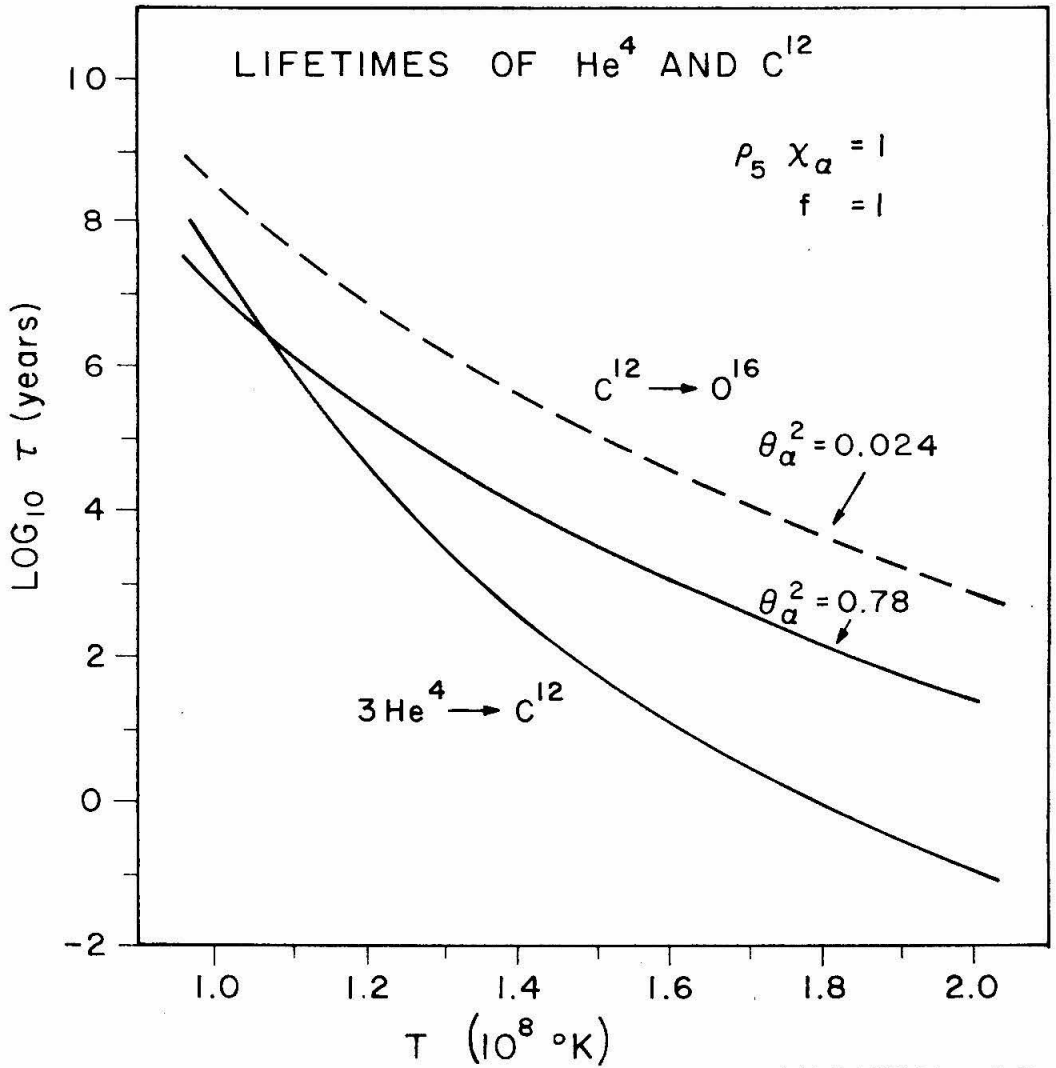


FIGURE 28.

Lifetimes of He^4 and C^{12}

The logarithm of the lifetime $\tau_{3\alpha}(\text{He}^4)$ for a He^4 nucleus in the 3α process is plotted as a function of temperature for $\rho_5 X_\alpha = 1$ and $f = 1$. (Curve labeled $3\text{He}^4 \rightarrow \text{C}^{12}$.) Also plotted is the lifetime $\tau_\alpha(\text{C}^{12})$ of a C^{12} nucleus undergoing He-burning, for two different assumptions of the width θ_α^2 of a level in O^{16} . The value 0.78 is preferred theoretically and astronomically. (See text p. 38.)